



Article

Phase–Frequency Cooperative Optimization of HMDV Dynamic Inertial Suspension System with Generalized Ground-Hook Control

Yihong Ping ¹, Xiaofeng Yang ¹, Yi Yang ², *, Yujie Shen ³, Shaocong Zeng ¹, Shihang Dai ¹ and Jingchen Hong ¹

- School of Automotive and Traffic Engineering, Jiangsu University, Zhenjiang 212013, China
- Department of Civil and Environmental Engineering, The Hong Kong Polytechnic University, Kowloon, Hong Kong 999077, China
- Automotive Engineering Research Institute, Jiangsu University, Zhenjiang 212013, China
- * Correspondence: yyi.yang@polyu.edu.hk

Abstract

Hub motor-driven vehicles (HMDVs) suffer from poor handling and stability due to an increased unsprung mass and unbalanced radial electromagnetic forces. Although traditional ground-hook control reduces the dynamic tire load, it severely worsens the body acceleration. This paper presents a generalized ground-hook control strategy based on impedance transfer functions to address the parameter redundancy in structural methods. A quarter-vehicle model with a switched reluctance motor wheel hub drive was used to study different orders of generalized ground-hook impedance transfer function control strategies for dynamic inertial suspension. An enhanced fish swarm parameter optimization method identified the optimal solutions for different structural orders. Analyses showed that the third-order control strategy optimized the body acceleration by 2%, reduced the dynamic tire load by 8%, and decreased the suspension working space by 22%. This strategy also substantially lowered the power spectral density for the body acceleration and dynamic tire load in the low-frequency band of 1.2 Hz. Additionally, it balanced computational complexity and performance, having slightly higher complexity than lower-order methods but much less than higher-order structures, meeting real-time constraints. To address time-domain deviations from generalized ground-hook control in semi-active systems, a dynamic compensation strategy was proposed: eight topological structures were created by modifying the spring-damper structure. A deviation correction mechanism was devised based on the frequency-domain coupling characteristics between the wheel speed and suspension relative velocity. For ride comfort and road-friendliness, a dual-frequency control criterion was introduced: in the low-frequency range, energy transfer suppression and phase synchronization locking were realized by constraining the ground-hook damping coefficient or inertance coefficient, while in the high-frequency range, the inertia-dominant characteristic was enhanced, and dynamic phase adaptation was permitted to mitigate road excitations. The results show that only the T0 and T5 structures met dynamic constraints across the frequency spectrum. Time-domain simulations showed that the deviation between the T5 structure and the third-order generalized groundhook impedance model was relatively small, outperforming traditional and T0 structures, validating the model's superior adaptability in high-order semi-active suspension.

Keywords: HMDV; generalized ground-hook control; vehicle dynamic inertial suspension; handling stability; phase deviation



Academic Editor: Raffaele Di Gregorio

Received: 19 May 2025 Revised: 19 June 2025 Accepted: 24 June 2025 Published: 26 June 2025

Citation: Ping, Y.; Yang, X.; Yang, Y.; Shen, Y.; Zeng, S.; Dai, S.; Hong, J. Phase–Frequency Cooperative Optimization of HMDV Dynamic Inertial Suspension System with Generalized Ground-Hook Control. *Machines* 2025, 13, 556. https:// doi.org/10.3390/machines13070556

Copyright: © 2025 by the authors. Licensee MDPI, Basel, Switzerland. This article is an open access article distributed under the terms and conditions of the Creative Commons Attribution (CC BY) license (https://creativecommons.org/licenses/by/4.0/).

Machines **2025**, 13, 556

1. Introduction

HMDVs [1,2], a significant technological innovation in electric vehicles [3–5], are regarded as the core direction of future electrification and intelligence due to their advantages, including a high energy conversion efficiency, compact structure, and fast dynamic response. Their application significantly enhances the vehicle handling performance [6–8] and range. However, the technology faces severe challenges from the adverse effects of vertical vibration in practical use: the integrated design of hub motors [9,10] leads to a significant increase in the unsprung mass, exacerbating the coupling effect between the dynamic tire load and road surface excitation, which in turn causes an increase in the root mean square value of body acceleration, directly reducing the vehicle ride comfort and passenger comfort.

In the field of vertical vibration control for HMDVs, the existing research has developed two major technical approaches: suspension structure optimization and control strategy innovation. Li [11] constructed a cooperative system of inertial suspension and ground-hook control based on positive fundamental network theory. Through genetic algorithm optimization, the root mean square (RMS) value of the body acceleration was reduced by 12.7%. However, its single-frequency band optimization characteristic led to a 9.3% deterioration in the dynamic tire load, exposing the limitations of synergy between traditional inertial components and semi-active control. Yang's particle swarm optimization study [12] showed that an L4 inertial suspension structure could reduce the dynamic tire load by 16.38%, but this was accompanied by a 14.2% increase in the suspension working space, revealing the theoretical defects of traditional inertial suspensions in terms of dynamic decoupling between the inertial and elastic terms.

In response to these challenges, the academic community has successively proposed two strategies: the lightweight design and layout optimization of hub motors. Lightweight design research [13] indicates that using a carbon fiber shell can reduce the unsprung mass by 18%, but at a significant increase in the material cost; a compact electromagnetic design, although reducing the mass by 9.7%, significantly increases the amplitude of electromagnetic force fluctuations. Regarding layout optimization [14], a symmetrical distributed layout reduces the PSD of vertical vibration by 21.4%. However, due to space constraints in the wheel hub, the unsprung mass in a practical implementation is still 28.6% higher than that of traditional drive forms. Although these methods can alleviate the primary vibration problems caused by the increase in the unsprung mass, they cannot eliminate the broadband coupling effect of electromagnetic excitation and road disturbances.

Innovating suspension design theory [15–17] constitutes the central challenge in achieving breakthroughs in HMDV vertical dynamics research [18–20]. Smith's inertial theory [21] broke the constraints of mechanical network topologies and led research on new dynamic inertial suspension structures. Based on this, this study innovatively proposes a high-order generalized ground-hook control strategy. Based on the frequency-domain analysis of a quarter-vehicle model, the third-order control achieved a 74.4% drop in the PSD of the body acceleration at the 1.2 Hz frequency point, with only a little increase in the algorithm complexity compared to traditional ground-hook control, yet achieved a record-breaking 94.3% reduction in the dynamic tire load. More importantly, phase response characteristic analysis revealed that this strategy expands the coupling vibration attenuation band between the body and wheels, significantly improving the existing optimal results, verifying the unique advantages of high-order impedance control in multi-physics field-coupled vibration regulation [22].

The traditional ground-hook damping control strategy, first proposed by Valášek [23], is based on the damping control of the unsprung mass, which is connected to an ideal ground through damping, constantly dissipating the energy from wheel vibrations. It is

Machines 2025, 13, 556 3 of 28

a semi-active control strategy for road adhesion, but it has many limitations. Therefore, this paper proposes a generalized ground-hook dynamic inertial suspension structure, elevating the ground-hook control theory to the level of mechanical networks. Based on mechanical impedance theory [24–26], a generalized ground-hook control theory was proposed, and a single-wheel model of the HMDV generalized ground-hook dynamic inertial suspension was established to explore the impact of the generalized ground-hook theory on HMDV suspension design. The objective was to mitigate the significant deterioration in the body acceleration caused by traditional ground-hook control strategies and further enhance the overall effectiveness of ground-hook control, thereby improving the overall performance of the HMDV suspension and enhancing both the ride comfort and handling stability. Due to the numerous components of the generalized ground-hook structure, which are challenging to implement in practical applications, impedance transfer functions were used to replace this complex and diverse structure.

Broadly defined, ground-hook control exhibits unique advantages in impedance regulation within suspension systems, but realizing the ideal inertial suspension requires mapping using control strategies. Active control [27-29], capable of precisely reproducing the target forces using electromagnetic actuators, is constrained by high energy consumption and phase mismatches caused by response lags. Semi-active control [30,31], which employs magnetorheological dampers to adjust the damping coefficients, significantly improves the energy efficiency while maintaining over 80% of the effectiveness of active control. This approach better aligns with the energy efficiency constraints of HMDV systems, leading to the selection of a semi-active structure for implementing broadly defined ground-hook control in this study. Continuous and dual-state (two-level) adjustable schemes present a technical trade-off regarding damping regulation mode selection. Continuously adjustable dampers [32-34] typically enable stepless variation in the damping coefficients within the range of 300–1500 N·s/m via proportional valves, allowing for the precise matching of the dynamic impedance curves required by broadly defined groundhook control. However, this scheme suffers from drawbacks such as overshoots due to dynamic response mismatches and the increased complexity of the hydraulic system, leading to higher costs and reduced reliability. In contrast, dual-state adjustable dampers [35], based on a high/low-damping-state switching mechanism using solenoid valves, exhibit significantly faster response speeds than continuously adjustable dampers, enabling precise synchronization with the phase characteristics of the transient impact conditions in suspension systems. Therefore, this study opted to use the dual-state adjustable damping mode.

In the semi-active control of traditional spring-damper parallel suspension systems, the fixed topological structure results in limited frequency-domain degrees of freedom, leading to deviation in the suspension performance indicators. To address this, this study introduces a multi-topological paradigmatic structure, whose core idea lies in leveraging the principle of analytic continuation from complex function theory to construct multiple suspension structures with distinct dynamic characteristics, thereby expanding the system's analytical dimensions in the frequency domain. Specifically, traditional suspensions are limited by their fixed topological structures, with the poles and zeros of their transfer functions being relatively concentrated, leading to an inability to flexibly match the control demands in terms of the phase response across a wide frequency range. To overcome this, eight transfer function matrices with different pole and zero structures were designed, equivalent to constructing multiple complementary analytic regions in the complex plane, each corresponding to the frequency-domain characteristics of a specific topology. By superposing these analytic regions in Hilbert space [36], the system can cover a broader frequency range and form a complementary mechanism for the phase response, thereby reducing the system deviations.

Machines 2025, 13, 556 4 of 28

The organizational structure of this paper is outlined as follows: First, Section 2 presents a quarter-vehicle dynamic model that incorporates switched reluctance motors, establishing a foundational framework for subsequent research. Next, Section 3 delves into the generalized mechanical network impedance transfer functions, starting with deriving the first-order to fifth-order generalized mechanical network impedance transfer functions. In Section 4, we describe how the generalized ground-hook dynamic inertial suspension system parameters, which included transfer functions of different orders, were optimized. Based on this, a comparative analysis assessed the optimization effects of different-ordered generalized mechanical network impedance transfer functions on the suspension performance indicators. We systematically performed time-domain and power spectral density frequency-domain analyses to explore the model characteristics and optimization effectiveness from multiple perspectives. Furthermore, Section 5 describes the implementation of semi-active control for the generalized ground-hook dynamic inertial suspension. Time-domain analysis revealed significant systematic deviations in the body acceleration, dynamic tire load, and suspension working space parameters following the application of the semi-active control strategy. In light of this, we expanded the traditional spring-damper parallel suspension structure into eight paradigmatic topological structures. The transfer functions for the relative velocities of the wheel speed and suspension motion were established for each structure, allowing for a systematic analysis of their phase-frequency response characteristics. Based on generalized ground-hook control logic screening, suitable paradigmatic structures were selected. Subsequently, time-domain analyses were conducted to identify the structure that most closely approximated the ideal generalized ground-hook control effect. Finally, Section 6 summarizes the key findings and conclusions of this study, offering insights for future research.

2. The Construction of a Hub Motor Dynamic Inertial Suspension Model

2.1. SRM Model

Figure 1a shows a single-wheel system of an HMDV; the corresponding structure of the hub motor-driven system is illustrated in Figure 1b. For the drive motor model, as depicted in Figure 1c [37], we utilized the widely researched switched reluctance motor (SRM) in this paper.

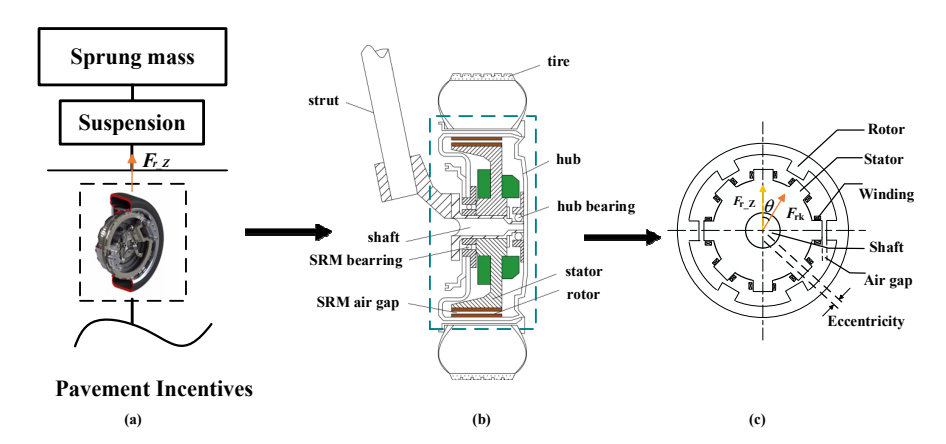


Figure 1. Drive system of a hub motor-driven vehicle: (a) quarter-HMDV single-wheel model, (b) the structure of the drive system for a hub motor-driven vehicle, (c) the structure of an 8/6-pole four-phase SRM with an external rotor [11].

2.2. The Construction of an Unbalanced Radial Electromagnetic Force Model for a Hub Motor

This paper first modeled the unbalanced radial electromagnetic forces in an SRM [38–40]. Building upon this foundation, electromagnetic, inductance, and unbalanced radial electro-

Machines **2025**, 13, 556 5 of 28

magnetic force equations were derived using Fourier series expansion [41] based on the virtual work principle [42–44].

The radial electromagnetic force F_r is given by

$$F_{\rm r} = \left. \frac{\partial W_{\rm m}}{\partial x} \right|_{i={\rm const}} = \int_0^i \frac{\partial \psi_k(\theta, i)}{\partial g_{\rm m}},\tag{1}$$

Here, $\psi_k(\theta, i)$ refers to the magnetic flux through a single pole of the motor. $W_{\rm m}$ refers to the magnetic energy.

The inductance of the winding for the phase *k* is

$$L_{k}(\theta, i) = \sum_{n=0}^{\infty} L_{n}(i_{k})\cos(nN_{r}\theta + \varphi_{n}) = \frac{1}{2} \left[\cos^{2}(N_{r}\theta) - \cos(N_{r}\theta)\right] \sum_{n=0}^{N} a_{n}i^{n}_{k} + \sin^{2}(N_{r}\theta) \sum_{n=0}^{N} b_{n}i^{n}_{k} + \frac{1}{2}L_{u} \left[\cos^{2}(nN_{r}\theta) + \cos(N_{r}\theta)\right]$$
(2)

Here, N_r represents the number of rotor poles of the motor; φ_n denotes the initial phase of each series term; L_n stands for the coefficient preceding each Fourier series term; L_u refers to the phase inductance when the stator and rotor salient poles are completely misaligned (at which point the phase inductance is at its minimum); and i_k is the current in the k phase winding.

The magnetic flux of the winding for the phase *k* is

$$\psi_{k}(\theta, i_{k}) = \int_{0}^{i} L_{k}(\theta, i_{k}) di_{k} = \frac{1}{2} \left[\cos^{2}(N_{r}\theta) - \cos(N_{r}\theta) \right] \sum_{n=0}^{N} c_{n} i^{n}_{k}
+ \sin^{2}(N_{r}\theta) \sum_{n=0}^{N} d_{n} i^{n}_{k} + \frac{1}{2} L_{u} i_{k} \left[\cos^{2}(nN_{r}\theta) + \cos(N_{r}\theta) \right]$$
(3)

In the formula, $c_n = a_n - n/1$ and $d_n = b_n - n/1$ are the integration coefficients for a_n and b_n , respectively.

The unbalanced radial force for the opposite pole of the phase *k* is

$$F_{\rm rk} = F_{\rm rm} - F_{\rm rn} = \frac{1}{2} i^2 {}_k \frac{L_k(\theta, i_k)}{l_{\rm g} + e} - \frac{1}{2} i^2 {}_k \frac{L_k(\theta + \pi, i_k)}{l_{\rm g} - e}, \tag{4}$$

For a four-phase switched reluctance motor, the total unbalanced radial electromagnetic force is

$$F_{r_{-}Z} = \sum_{k=1}^{4} F_{rk_{-}Z} = \sum_{k=1}^{4} F_{rk} \cos \theta, \tag{5}$$

In the formula, $F_{\rm rk_Z}$ represents the unbalanced radial electromagnetic force of the k phase. In addition, the magnitude of the unbalanced radial forces directly depends on the size of the eccentricity gap [45–47]. Road excitation easily influences this gap, thereby worsening the vehicle's ride comfort and handling stability.

3. The Construction of an HMDV Dynamic Inertial Suspension Model Based on the Generalized Ground-Hook Theory

3.1. Generalized Ground-Hook Theory

The ground-hook damping suspension control strategy aims to reduce the suspension working space and the force between the road and the tire by adding a damping element connecting the wheel to the ideal ground. However, since the ground-hook damping theory is a suspension design method based on an ideal structure, it is not feasible to implement ground damping in vehicles.

Machines **2025**, 13, 556 6 of 28

The generalized ground-hook theory is an extension of the traditional ground-hook damping theory. In the generalized ground-hook theory, the traditional spring–damper element system is generalized as T(s). The traditional ground-hook damping element is generalized as an impedance transfer function K(s). One end of the impedance transfer function K(s) is connected to the ideal ground and the other to the unsprung mass. The following equation can express the impedance function:

$$Y(s) = F(c_{gnd-i}, \frac{k_{gnd-i}}{s}, b_{gnd-i}s), \tag{6}$$

$$T(s) = F(c_i, \frac{k_i}{s}, b_i s), \tag{7}$$

where i = 1,2,3..., represents the sequence number of the mechanical elements, k_{gnd-i} denotes the ground-hook spring stiffness, c_{gnd-i} denotes the ground-hook damping coefficient, and b_{gnd-i} denotes the ground-hook inertial coefficient.

3.2. A Quarter Model of an HMDV Dynamic Inertial Suspension Based on the Generalized Ground-Hook Theory

Combining generalized semi-active suspension with an HMDV structure represents an innovative vehicle suspension system design approach. The core of this design lies in optimizing the suspension system's dynamic characteristics to effectively control the dynamic tire loads and body accelerations, thereby suppressing vibrations. This design reduces the vehicle's impact on the road surface during travel and mitigates the body vibrations caused by road irregularities, significantly enhancing the vehicle's handling stability and ride comfort.

Table 1 presents the specifications for an in-wheel motor dynamic inertia suspension. We selected the GAC Trumpchi GS4 vehicle model as a reference for formulating the relevant parameters. The characteristic frequency of this suspension is 1.32 Hz, and the dimensionless damping coefficient of the passive suspension is 0.283.

Parameter	Value	
Sprung mass	$m_{\rm s}/({\rm kg})$	320
Stator mass of the motor	$m_{\rm us}/({\rm kg})$	45
Rotor mass of the motor	$m_{\rm es}/({\rm kg})$	30
Suspension spring stiffness	k/(N/m)	22,000
Tire equivalent stiffness	$k_{\rm t}/({\rm N/m})$	190,000
Motor equivalent stiffness	$k_{\rm m}/({\rm N/m})$	3,850,000
Suspension damping coefficient	$c/(N\cdot s/m)$	1500
Motor clearance	$l_{\rm g}/({\rm mm})$	0.5

Table 1. Table of the parameters of a hub motor dynamic inertial suspension.

Figure 2a shows the quarter-vehicle suspension model based on the impedance transfer function within the generalized ground-hook theory, while Figure 2b shows the corresponding spring-damper suspension system model employing the same theory.

Machines **2025**, 13, 556 7 of 28

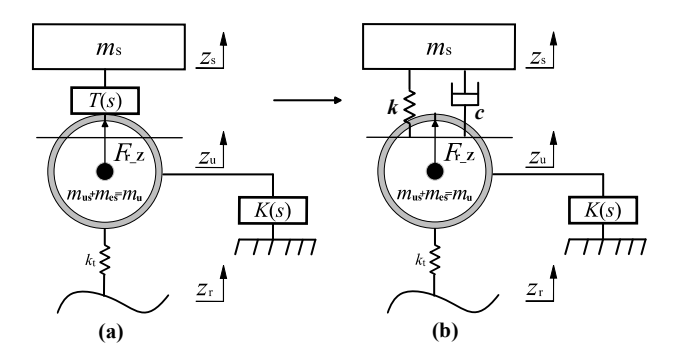


Figure 2. (a) Quarter-vehicle suspension model based on the impedance transfer function in the generalized ground-hook theory. (b) Quarter-vehicle suspension model of a spring-damper suspension system using the generalized ground-hook theory.

The dynamic equations for the structure depicted in Figure 2b are derived as follows:

$$\begin{cases}
 m_{s}\ddot{z}_{s} + k(z_{s} - z_{u}) + c(\dot{z}_{s} - \dot{z}_{u}) = 0 \\
 (m_{us} + m_{es})\ddot{z}_{u} + k_{t}(z_{u} - z_{r}) - k(z_{s} - z_{u}) - c(\dot{z}_{s} - \dot{z}_{u}) + K_{s}\dot{z}_{u} + F_{r} = 0'
\end{cases}$$
(8)

In Equation (8), z_s , z_u , and z_r represent the vertical displacements of the sprung mass, unsprung mass, and road surface, respectively; F_{r_z} denotes the unbalanced electromagnetic radial force.

Compared to traditional ground-hook dynamic inertial suspensions, the generalized ground-hook dynamic inertial suspension has significantly expanded application boundaries achieved through systematic upgrades. Its core innovation lies in establishing a high-order system design framework based on impedance transfer functions. After completing the structural topology optimization design, impedance transfer functions can be introduced as a system characterization tool to analyze complex high-order generalized ground-hook systems containing multiple components effectively. This method [48] relies on electromechanical similarity theory to transform the dynamic characteristics of mechanical networks into impedance transfer function expressions. All the mechanical network structures associated with the studied orders can be comprehensively encompassed solely by setting the order of the impedance transfer function. This is ultimately passively realized using passive network synthesis theory, combined with mathematical tools such as parameter optimization algorithms or linear matrix inequalities (LMIs) for global optimization [49].

Furthermore, this method breaks through the numerous limitations of traditional designs during implementation. Unlike traditional suspension design paradigms based on impedance transfer functions, the generalized ground-hook system allows partial mechanical networks to exist in virtually ground-connected forms, eliminating the mandatory requirement for basic components such as support springs. This enhancement of the topological degrees of freedom expands the design space and bypasses complex topological derivation steps in traditional network synthesis through direct impedance function parameterization. The resulting vibration isolation networks maintain equivalent dynamic characteristics while presenting simpler physical implementations, significantly enhancing their practicality.

Equations (9)–(13) list the forms of the first-order, second-order, third-order, fourth-order, and fifth-order impedance transfer functions, respectively, according to the order of the impedance transfer function.

$$K_1(s) = b_1 \frac{s + b_0}{s + a_0},\tag{9}$$

Machines **2025**, 13, 556 8 of 28

$$K_2(s) = b_2 \frac{s^2 + b_1 s + b_0}{s^2 + a_1 s + a_0},\tag{10}$$

$$K_3(s) = b_3 \frac{s^3 + b_2 s^2 + b_1 s + b_0}{s^3 + a_2 s^2 + a_1 s + a_0},$$
(11)

$$K_4(s) = b_4 \frac{s^4 + b_3 s^3 + b_2 s^2 + b_1 s + b_0}{s^4 + a_3 s^3 + a_2 s^2 + a_1 s + a_0},$$
(12)

$$K_5(s) = b_5 \frac{s^5 + b_4 s^4 + b_3 s^3 + b_2 s^2 + b_1 s + b_0}{s^5 + a_4 s^4 + a_3 s^3 + a_2 s^2 + a_1 s + a_0},$$
(13)

Here, a_0 , a_1 , a_2 , a_3 , a_4 , b_0 , b_1 , b_2 , b_3 , b_4 and b_5 are coefficient terms, and s is the Laplace variable.

4. The Parameter Optimization of the Impedance Transfer Function for the Generalized Ground-Hook Dynamic Inertial Suspension and Its Order Selection

4.1. The Parameter Optimization of the Impedance Transfer Function for the Generalized Ground-Hook Dynamic Inertial Suspension

As a novel vibration control device, the generalized ground-hook dynamic inertial suspension system exhibits dynamic characteristics determined by the synergistic effects of multiple physical components such as springs, dampers, and inerters. The system can efficiently absorb vibrational energy and precisely control the frequency-domain response by adjusting the order and parameters of K(s). Research has shown that the order of the impedance transfer function directly influences the system's dynamic characteristics: while low-order models are simple in structure and easy to implement, their frequency band control capabilities are limited, making it challenging to suppress wide-frequency-range vibrations; high-order models (such as fourth-order models and above) can significantly enhance the low-frequency anti-resonance and high-frequency attenuation performance by introducing additional poles and zeros, but they also increase the system complexity and parameter sensitivity. However, the selection of the order requires a balance between the system performance and implementation cost, with sensitivity manifested in the following ways: if the order is too high, it may lead to parameter redundancy, decreased stability, and difficulties in controller design; if the order is insufficient, it may fail to meet the dynamic performance requirements under multiple operating conditions.

The traditional structural method constructs global equations of motion by analyzing the force relationships of various components in the system, providing a complete depiction of the physical structural details of the suspension system. However, its limitations in dynamic modeling and optimization design significantly constrain its efficiency in practical applications. Firstly, the structural method requires the explicit consideration of all the degrees of freedom and nonlinear coupling terms, leading to an exponential increase in the dimensions of differential equations with increasing system complexity. More crucially, the order of the structural method model is passively determined by the inherent properties of the physical structure and cannot be actively adjusted based on the performance requirements.

In contrast, the impedance method represents the system's input—output relationship as a complex frequency-domain rational fraction. The proper response within critical frequency bands is approximated using low-order models, achieving model order reduction and frequency-domain characteristic focusing by rationally selecting the transfer function order. Furthermore, the impedance method allows for the active adjustment of the model orders based on the optimization requirements. While ensuring low-frequency accuracy, forming a flexible "on-demand modeling" framework, this order controllability provides

Machines 2025, 13, 556 9 of 28

efficient collaborative optimization pathways for intelligent algorithms like fish swarm optimization, enabling simultaneous searches for optimal order–parameter combinations. This avoids the issues present in traditional structural methods, such as the insufficient model expressiveness caused by fixed-order constraints.

This study employed a modified artificial fish swarm algorithm [50,51] for suspension parameter optimization design. The algorithm effectively addressed the challenges of multivariable collaborative optimization and initial value uncertainty in the impedance transfer function. To establish a comparative analysis framework while maintaining consistent baseline suspension parameters, we took traditional passive suspension and traditional ground-hook control suspension as references. The focus was on the multi-objective optimization of the numerator and denominator coefficients in the generalized ground-hook system's impedance transfer function K(s). Constructing a normalized evaluation function [52] incorporating the root mean square (RMS) values of the body acceleration, suspension working space, and dynamic tire load, the multi-performance collaborative optimization problem was transformed into a weighted sum minimization problem based on the road excitation's spectral characteristics and vehicle's dynamic responses. The mathematical formulation is expressed as

$$\min F_i = \alpha_1 \frac{BA_i(P_i)}{BA_{\text{pas}}} + \alpha_2 \frac{SWS_i(P_i)}{SWS_{\text{pas}}} + \alpha_3 \frac{DTL_i(P_i)}{DTL_{\text{pas}}},$$
(14)

where α_1 , α_2 , and α_3 are the weight coefficients and BA_{pas} , SWS_{pas} , and DTL_{pas} represent the root mean square values of the body acceleration, suspension working space, and dynamic tire load for the traditional suspension, respectively. This strategy retained the comparability of the suspension's mechanical parameters while achieving the targeted optimization of dynamic characteristics by adjusting the degrees of freedom of the impedance function, thereby avoiding the interference of structural parameter differences in the performance evaluation.

 P_i represents the set of parameters to be optimized (i = 1, 2, 3, 4, 5), and i indicates the sequence of the inertial suspension S_i to be optimized (when i = 1, it represents the optimization of the parameters of the S1 inertial suspension). The generalized ground-hook dynamic inertial suspension parameters that needed to be optimized were the coefficients of the numerator and denominator of the impedance transfer function K(s), all of which needed to satisfy the condition of being greater than zero. The optimal solution obtained through algorithm optimization is shown in Table 2.

Table 2. Table of the optimized S1, S2, S3, S4, and S5 structures of the generalized ground-hook dynamic inertial suspension parameters.

Optimized Parameters	S1	S2	S3	S4	S 5
a_0	4989.2	3138.1	3698.1	1450.2	3029.9
a_1		4983	9216	3150	1271.6
a_2			16,598	3879.2	3130.5
a_3				5000	632.5
a_4					4974.7
b_0	10	560.2	2400	868.3	2118
b_1	606.1	5	5	1484.7	1438.2
b_2		313	365.6	1023.8	2416.7
b_3			20.3	5	524.3
b_4				626.1	5
b_5					12.1

Machines **2025**, 13, 556

4.2. The Selection of the Order for the Impedance Transfer Function of a Generalized Ground-Hook Dynamic Inertial Suspension

4.2.1. Time-Domain Analysis

A simulation analysis used a class C road surface [53] as the input and a constant vehicle speed of 20 m/s. The results are shown in Figure 3, where a, b, and c represent the time-domain plots of the body acceleration, dynamic tire load, and suspension working space for the first-order to fifth-order generalized ground-hook impedance transfer function control suspensions (hereinafter referred to as first-order to fifth-order generalized ground-hook control suspensions).

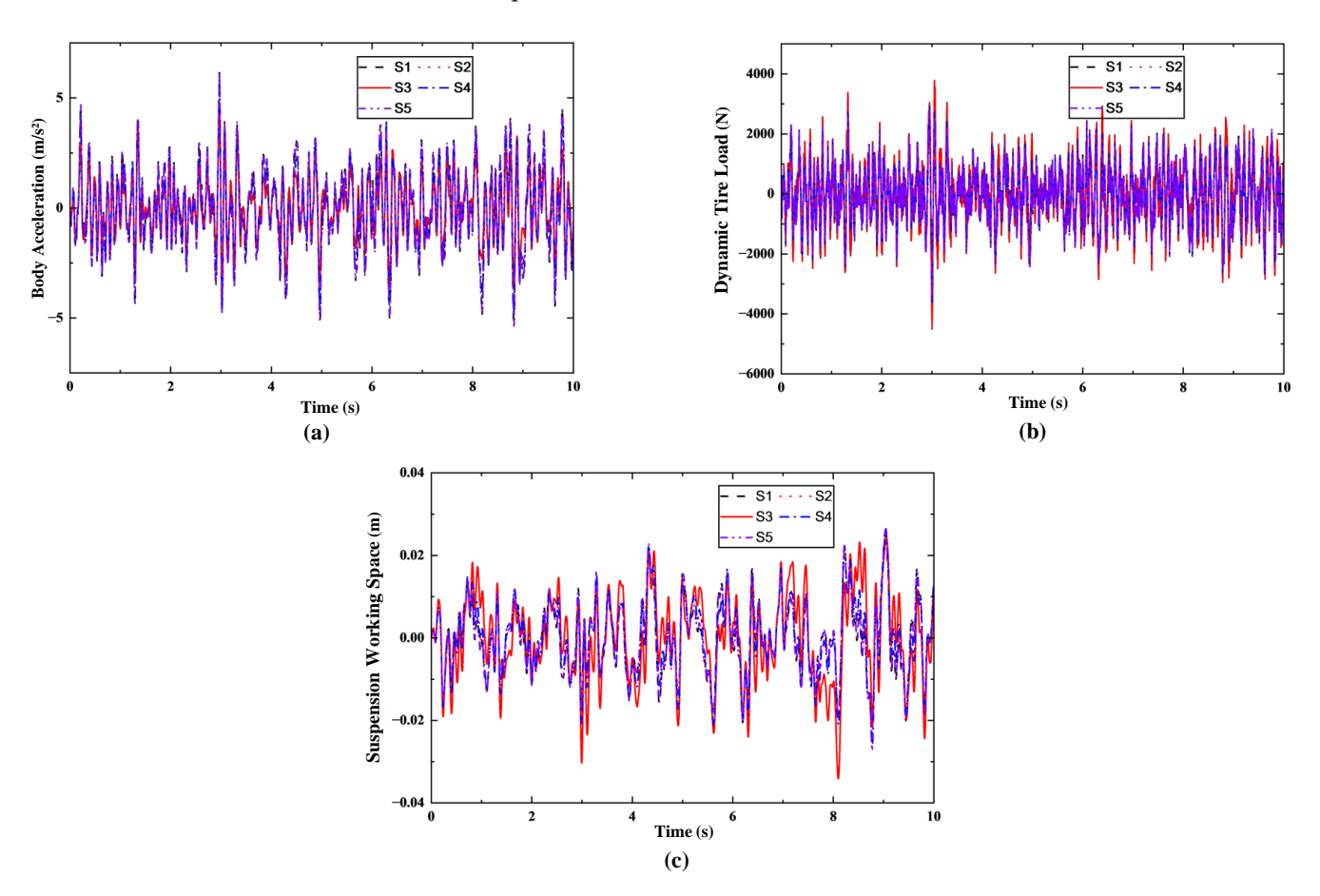


Figure 3. Time-domain comparison of suspension performance for first-order to fifth-order generalized ground-hook control under random road conditions: (a) body acceleration, (b) dynamic tire load, (c) suspension working space.

From the results shown in Figure 3, the time-domain response characteristics of the body acceleration, dynamic tire load, and suspension working space reveal the impact of different orders of the generalized ground-hook impedance transfer function on the suspension performance. As can be seen from the time-domain plot of the body acceleration, with an order increasing from the first to the third, the acceleration amplitude decreased significantly, indicating that the third-order transfer function could effectively suppress the vertical vibration of the vehicle body and improve the ride comfort. The improvement in the acceleration for the fourth and fifth orders tended to level off, suggesting that higher-order transfer functions offered limited marginal gains in comfort. The time-domain fluctuations in the dynamic tire load stabilized at the third order, with a noticeably reduced fluctuation range, indicating that the third-order transfer function had an advantage in stabilizing the tire ground force, avoiding grip instability caused by sudden load changes and thus enhancing the vehicle handling stability. The time-domain curve of the suspension working

Machines 2025, 13, 556 11 of 28

space shows that the third-order transfer function could control the suspension working space within a reasonable range, avoiding the risk of the suspension bottoming out and reducing the energy loss from high-frequency, small-amplitude oscillations. Higher-order (such as S4 and S5) improvements in the suspension working space were not significant and may even lead to control delays due to increased algorithm complexity, which is detrimental to the dynamic response. Furthermore, the third-order transfer function has moderate structural complexity, with only a slight increase in algorithmic computation compared to the first and second orders and a much lower increase compared to the fourth and fifth orders. It can meet real-time control requirements while reducing the hardware implementation costs. Therefore, the third-order generalized ground-hook impedance transfer function achieves an optimal balance between comfort, handling stability, suspension safety, and practical feasibility, making it a reasonable choice that balances performance and complexity.

Now, the control strategy of the third-order generalized ground-hook impedance transfer function is compared with the traditional passive suspension and the traditional ground-hook damping control strategy. The traditional ground-hook damping coefficient $c_{\rm gnd}$ was 200 N·s/m. (S1, S2, S3, S4, and S5 represent the first-order to fifth-order generalized ground-hook control suspensions, passive represents passive suspension, and Trad-GH represents traditional ground-hook control suspension).

Based on the results shown in Figure 4, under the simulation conditions of a class C road input and a constant vehicle speed of 20 m/s, the time-domain response characteristics of the passive suspension, the traditional ground-hook control suspension, and the third-order generalized ground-hook control suspension were compared, as shown in Figure 4a-c. The impacts on the vehicle comfort and handling stability could be analyzed explicitly in the transient and steady-state stages. During the transient response stage from 0 to 3 s, the peak body acceleration of the traditional ground-hook control reached up to 7 m/s², with slow vibration decay exhibiting significant low-frequency oscillation characteristics; the dynamic tire load of the passive suspension fluctuated within a range of nearly ± 5000 N, accompanied by suspension working space fluctuations reaching ± 0.03 m, revealing significant risks of transient instability. However, leveraging the high-frequency attenuation capability of the third-order impedance transfer function, S3 suppressed the acceleration peak to within 3 m/s² while achieving dual coordinated control of the dynamic tire load amplitude and suspension working space, stabilizing them within ± 3000 N and ± 0.02 m, respectively. This optimized the tire ground contact performance through dynamic load balancing, significantly enhancing the comfort and handling stability under transient conditions. During the steady-state response stage from 8 to 10 s, the maximum fluctuation in the body acceleration of the traditional ground-hook control still reached ±5 m/s²; the dynamic tire load fluctuation of the passive suspension remained close to ± 4000 N, causing continuous bumping and unstable tire adhesion. The suspension working space frequently reached the ± 0.04 m limit, posing a risk of bottoming out. However, S3 further reduced the acceleration to below 1 m/s² and stabilized the dynamic load fluctuation within ± 1500 N. Compared with traditional solutions, the improvement was significant. Its multi-frequency-band coordinated control effectively isolated medium-frequency and high-frequency road excitations, and its uniform spectral distribution ensured long-term riding comfort. At the same time, optimizing the distribution of the tire ground force through impedance matching significantly enhanced the directional stability at high speeds.

Machines **2025**, 13, 556

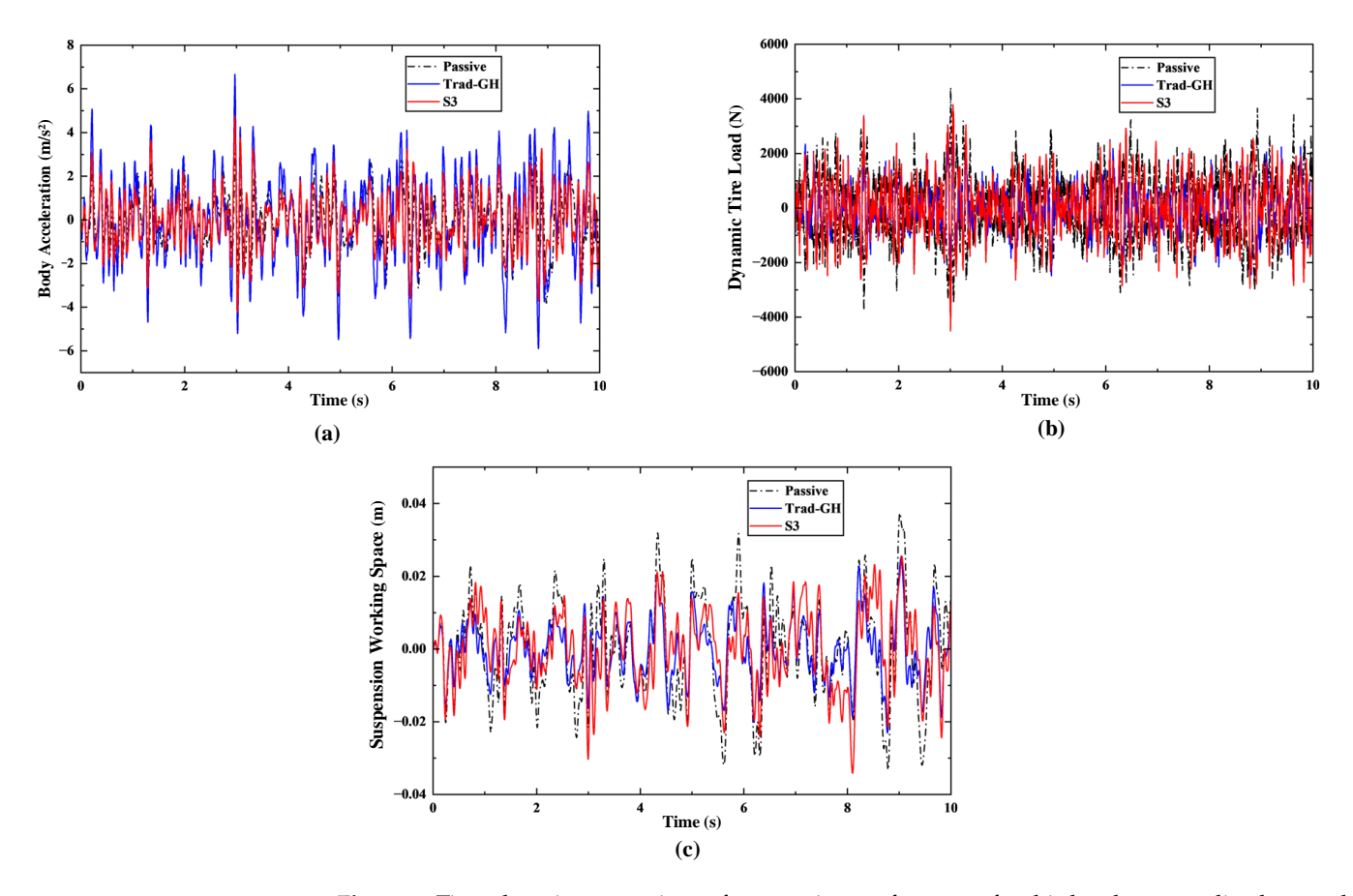


Figure 4. Time-domain comparison of suspension performance for third-order generalized ground-hook control suspension, traditional passive suspension, and traditional ground-hook damping control suspension under random road conditions: (a) body acceleration, (b) dynamic tire load, (c) suspension working space.

S3, due to the phase compensation characteristics of its third-order impedance transfer function, achieved the full time-domain suppression of the body acceleration and dynamic load balancing without significantly increasing the algorithmic complexity. It compressed the suspension working space amplitude into a safe range to reduce the system fatigue damage. It balanced the transient convergence speed and steady-state control accuracy through high-frequency attenuation and mid-frequency impedance matching. Compared with traditional passive suspension and ground-hook control, it achieved a better synergistic balance between the comfort, handling stability, and practical feasibility, making it an ideal suspension control strategy to allow HMDVs to cope with class C road excitations.

Since there were significant differences in the magnitude between the dynamic tire load and the body acceleration values, as shown in Table 3, making it difficult to comprehensively evaluate the merits and demerits of these three performance indicators on a single graph, the optimized values of the suspension performance indicators for each control strategy were divided by the values of the corresponding indicators for the traditional passive suspension, as shown in Figure 5, facilitating the selection of the optimal control strategy.

Figure 5 systematically compares the changes in the suspension dynamic characteristics under traditional passive suspension, traditional ground-hook damping control, and first-order to fifth-order generalized ground-hook control strategies. The data shows that as the order of the generalized ground-hook impedance transfer function increased, the system exhibited significant nonlinear optimization characteristics: The third-order generalized ground-hook control achieved the optimization of the dynamic tire load and suspension working space, with reductions of 8% and 22%, respectively, while maintaining

Machines **2025**, 13, 556

a slight improvement of 2% in the body acceleration. Notably, although the fourth-order and fifth-order strategies exhibited better performance in dynamic tire load control (with S5 reaching a dynamic tire load of 861.76 N), their body acceleration indicators deteriorated to 1.7772 m/s², a 40.9% worsening compared to those for S3. This phenomenon reveals an inherent contradiction in the frequency-domain regulation of high-order impedance transfer functions—the cumulative effect of phase delays lead to a decrease in the high-frequency energy attenuation capability, resulting in the significant degradation of the acceleration indicators. In contrast, although traditional ground-hook damping control can effectively suppress the deterioration of the dynamic tire load, it is inferior to the S3 solution in optimizing the suspension working space and body acceleration, verifying the unique advantages of the third-order impedance network in the pole placement of the transfer function. Research indicates that the third-order generalized ground-hook impedance transfer function demonstrates unique advantages in terms of its dynamic response precision and multi-physics collaborative control.

Table 3. Performance comparison of first-order to fifth-order generalized ground-hook control suspensions on random roads.

Suspension Type	Performance Parameters						
	BA/(m/s ²)	Improvement	SWS/(m)	Improvement	DTL/(N)	Improvement	
Passive	1.2866	0	0.0135	0	1122.9	0	
Trad-GH	1.9077	-48%	0.0083	38%	878.05	22%	
S1	1.7772	-38%	0.0085	37%	861.8	23%	
S2	1.6126	-25%	0.0090	33%	889.3	21%	
S3	1.2614	2%	0.0105	22%	1030.3	8%	
S4	1.621	-26%	0.0089	34%	887.49	21%	
S5	1.7676	-37%	0.0085	37%	863.1	23%	

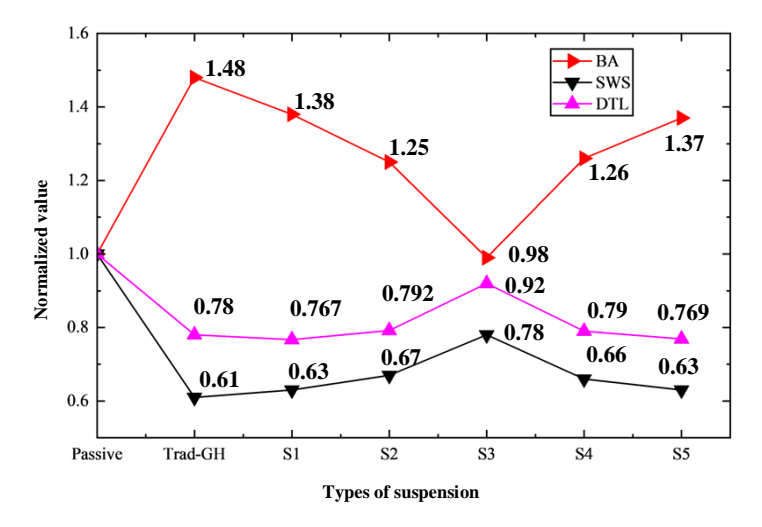


Figure 5. Comparison chart of three suspension performance indicators for traditional passive suspension, traditional ground-hook damping control, and first-order to fifth-order generalized ground-hook control strategies under random road conditions.

4.2.2. Power Spectral Density Frequency-Domain Analysis

The frequency-domain performance of traditional passive suspension, traditional ground-hook damping control, and suspension control under the first-order to fifth-order generalized ground-hook impedance transfer functions was simulated using the power spectral density of the body acceleration, the suspension working space density, and the dynamic tire load power spectral density as system performance indicators. The results are shown in Figures 6–9.

Machines 2025, 13, 556 14 of 28

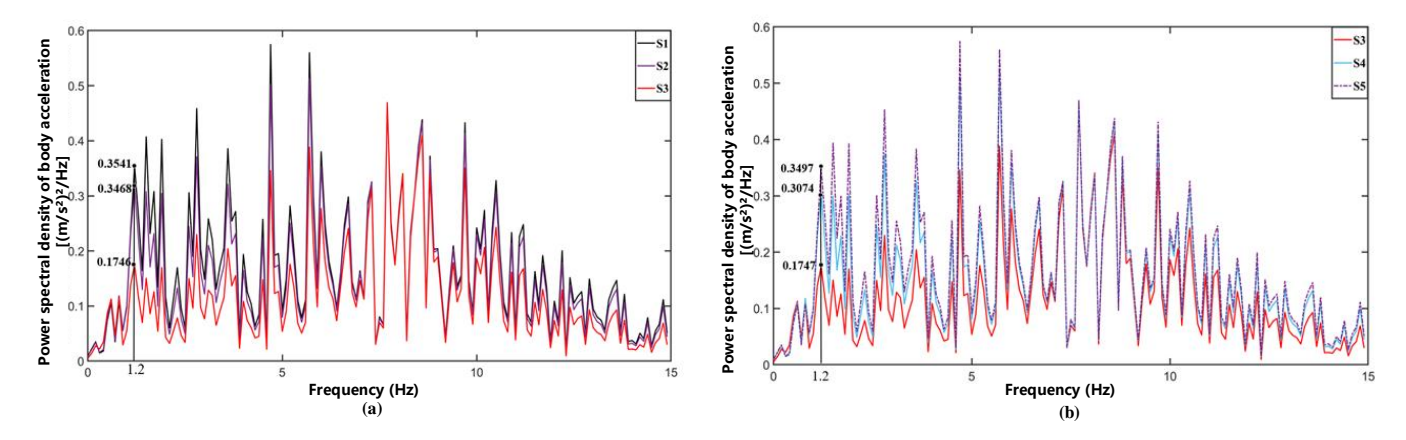


Figure 6. Comparison in the frequency domain of the power spectral density of the body acceleration for first-order to fifth-order generalized ground-hook control under random road conditions: (a) first-order to third-order, (b) third-order to fifth-order.

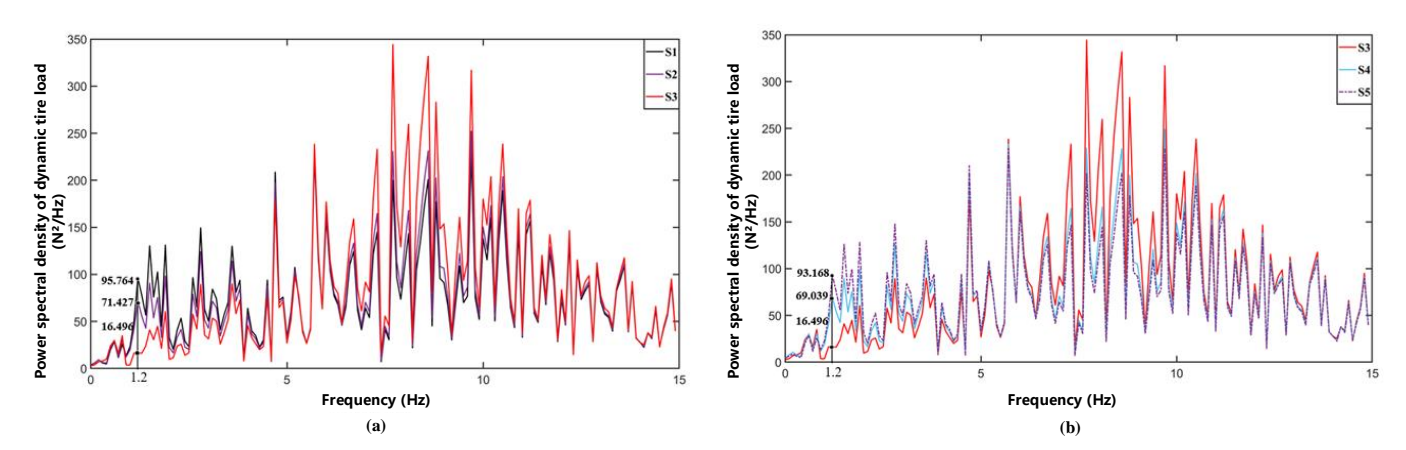


Figure 7. Comparison in the frequency domain of the power spectral density of the dynamic tire load for first-order to fifth-order generalized ground-hook control under random road conditions: (a) first-order to third-order, (b) third-order to fifth-order.

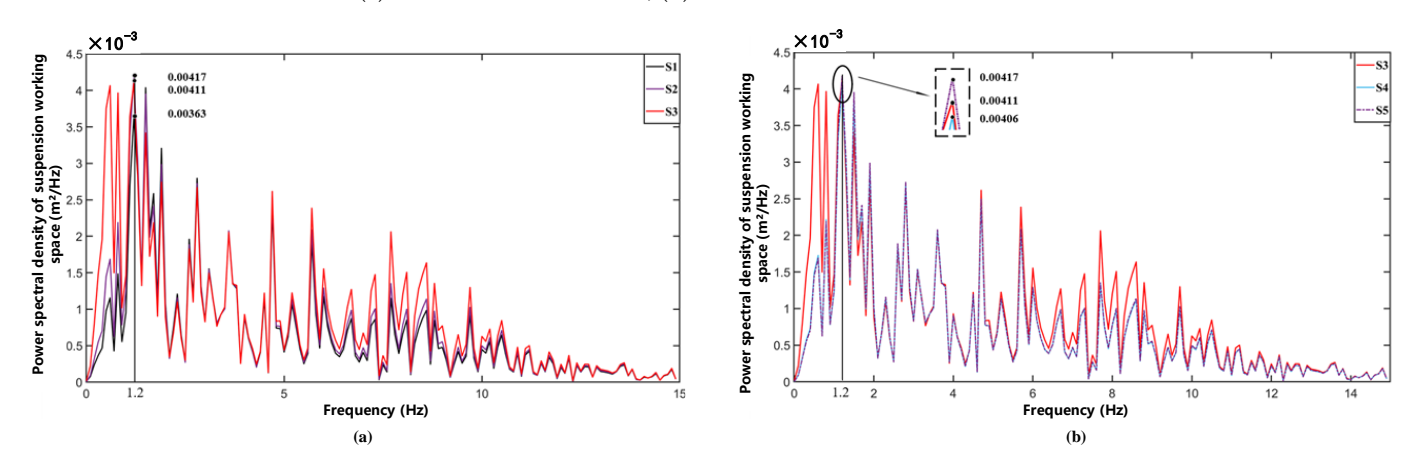


Figure 8. Comparison in the frequency domain of the power spectral density of the suspension working space for first-order to fifth-order generalized ground-hook control under random road conditions: (a) first-order to third-order, (b) third-order to fifth-order.

Machines **2025**, 13, 556 15 of 28

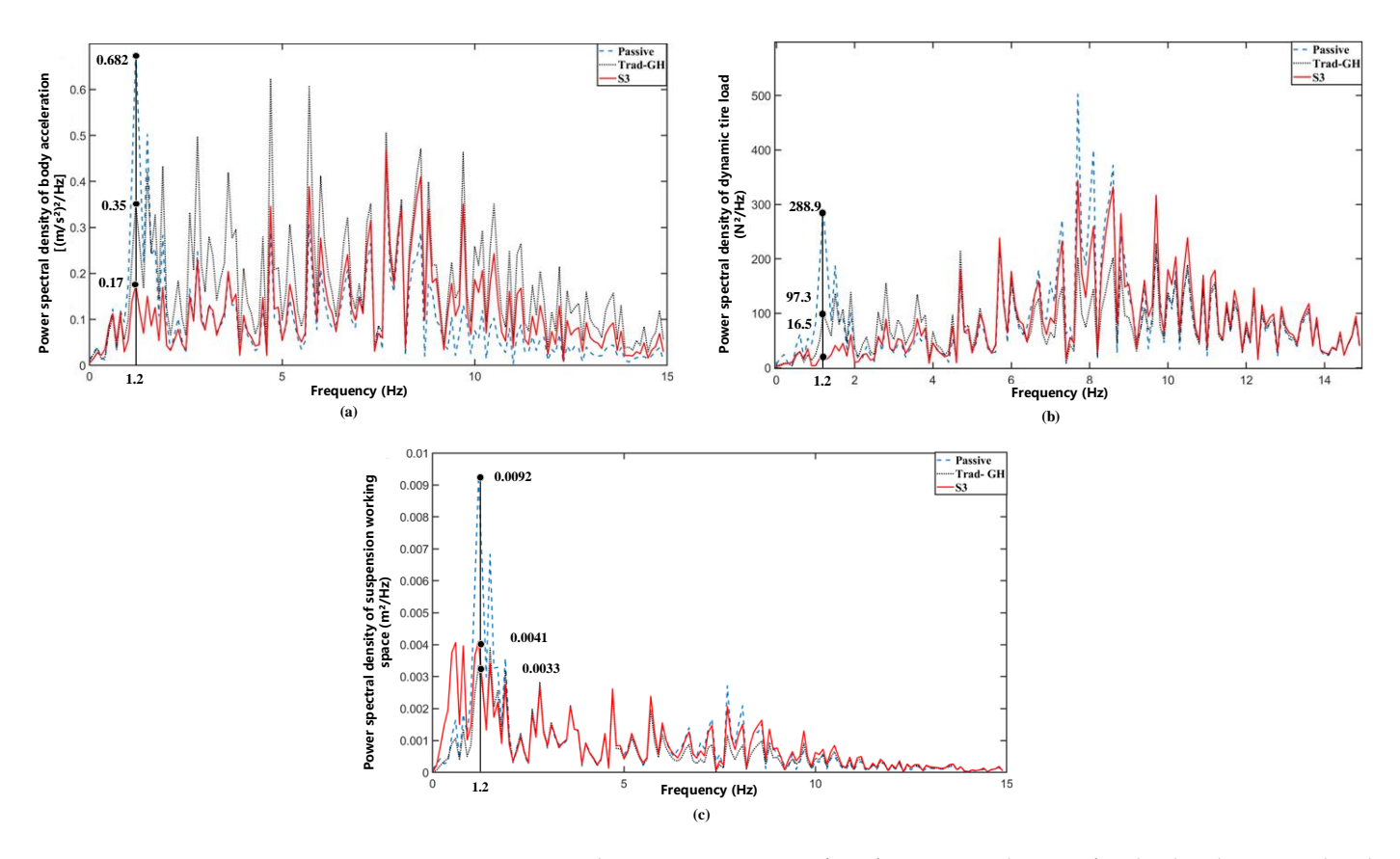


Figure 9. Frequency-domain comparison of performance indicators for third-order generalized ground-hook control suspension, traditional passive suspension, and traditional ground-hook damping control suspension under random road conditions: (a) body acceleration, (b) dynamic tire load, (c) suspension working space.

A comparison of the power spectral density (PSD) data in the 1.2 Hz low-frequency band revealed that the third-order generalized ground-hook impedance transfer function demonstrated significant comprehensive advantages in the multi-objective optimization of vehicle suspension systems. Among the first-order to fifth-order models, the third-order model reduced the body acceleration power spectral density to 0.1746 (m·s $^{-2}$)²/Hz, which represents a 50.7% improvement compared to the first-order model's 0.354 (m·s $^{-2}$)²/Hz and a 44.7% improvement compared to the second-order model's 0.316 (m·s $^{-2}$)²/Hz. It also significantly outperformed the fourth-order model's 0.307 (m·s $^{-2}$)²/Hz and the fifth-order model's 0.34967 (m·s $^{-2}$)²/Hz, indicating stronger robustness in suppressing vertical vibration energy transmission.

In the dynamic tire load index, the third-order model exhibited a power spectral density of only $16.496~N^2/Hz$, representing improvements of 82.8%, 76.9%, 76.1%, and 82.3% compared to the first-order model's $95.764~N^2/Hz$, the second-order model's $71.427~N^2/Hz$, the fourth-order model's $69.04~N^2/Hz$, and the fifth-order model's $93.1675~N^2/Hz$, respectively. This remarkable phenomenon reveals that its third-order dynamic structure possesses stronger attenuation capabilities for high-frequency disturbances in the tire–ground contact forces, significantly enhancing the vehicle driving safety.

In Figure 6, it can be seen that the vibration amplitude of the body acceleration significantly increased within the frequency range of 4–8 Hz. This indicates that the natural frequency of the vehicle body system resonated with the external excitation frequency within this frequency band, leading to energy concentration and a substantial increase in the vehicle body's vibration amplitude. Consequently, this adversely affected the ride comfort and stability. Similarly, in Figure 7, the dynamic tire load also shows a noticeable

Machines 2025, 13, 556 16 of 28

increase in the vibration amplitude within the 4–8 Hz range. This was attributed to the coupling effect between the tires and the suspension system, which resonated within this frequency band, resulting in energy accumulation and severe fluctuations in the tire load. This, in turn, impacted the vehicle's handling stability.

Although the differences in the suspension working space between the third-order model ($0.00417~\text{m}^2/\text{Hz}$) and the second-order model ($0.00417~\text{m}^2/\text{Hz}$), as well as the fourth-order model ($0.00406~\text{m}^2/\text{Hz}$), were minimal, their collaborative optimization effect on the body acceleration and dynamic tire load far surpassed those of the other orders. This indicates that the third-order transfer function achieves the nonlinear decoupling control of key dynamic parameters while maintaining the suspension geometric constraints through more precise frequency-domain characteristic matching. Notably, the performance degradation observed in higher-order models (such as the fifth-order model) suggests that excessive increases in the system complexity may introduce additional resonant modes. In contrast, the third-order model balances the model's complexity and dynamic performance through optimal order selection, thereby validating its structural superiority in low-frequency vibration suppression.

As can be seen from Figure 9, in the 1.2 Hz low-frequency band, the suspension controlled by the third-order generalized ground-hook impedance transfer function exhibited significant improvements compared to the traditional passive suspension. The body acceleration power spectral density decreased from 0.6824 (m·s $^{-2}$)²/Hz in the traditional suspension to 0.1746 (m·s $^{-2}$)²/Hz, representing 74.4% optimization. The dynamic tire load power spectral density decreased from 288.915 N²/Hz in the traditional suspension to 16.496 N²/Hz, achieving 94.3% optimization. The suspension working space power spectral density decreased from 0.00926 m²/Hz in the traditional suspension to 0.00417 m²/Hz, indicating 54.97% optimization. Compared to the suspension controlled by the traditional ground-hook damping, the body acceleration power spectral density decreased from 0.3491 (m·s $^{-2}$)²/Hz to 0.1746 (m·s $^{-2}$)²/Hz, representing 49.99% optimization. The dynamic tire load power spectral density decreased from 97.314 N²/Hz in the traditional ground-hook damping control suspension to 16.496 N²/Hz, achieving 83.05% optimization.

It can be seen that compared to the traditional ground-hook damping control suspension, the first-order, second-order, fourth-order, and fifth-order generalized ground-hook control suspensions, particularly the third-order one, significantly reduced the body acceleration, suspension working space, and dynamic tire load within the 0~2 Hz range. This optimization effect primarily stemmed from the more ideal amplitude–frequency attenuation characteristics of the third-order transfer function in the low-frequency range, where its phase compensation mechanism effectively balanced the energy transfer relationship between the sprung and unsprung masses. Compared to other higher-order models, the third-order generalized ground-hook impedance transfer function control strategy exhibited better overall performance, providing a new technical pathway for the coordinated control and improvement of the vehicle ride comfort and handling stability.

5. The Specific Implementation of the HMDV Generalized Ground-Hook Dynamic Inertial Suspension

5.1. Semi-Active Control of HMDV Generalized Ground-Hook Dynamic Inertial Suspension

Since the ideal generalized ground-hook dynamic inertial suspension system cannot be directly applied in vehicles, this paper proposes a new semi-active control method based on the generalized ground-hook impedance transfer function to achieve generalized ground-hook control. Figure 10a shows the ideal quarter-vehicle suspension model based on the impedance transfer function for the third-order generalized ground-hook, while Figure 10b shows the practical quarter-vehicle suspension model for the generalized ground-hook.

Machines **2025**, 13, 556 17 of 28

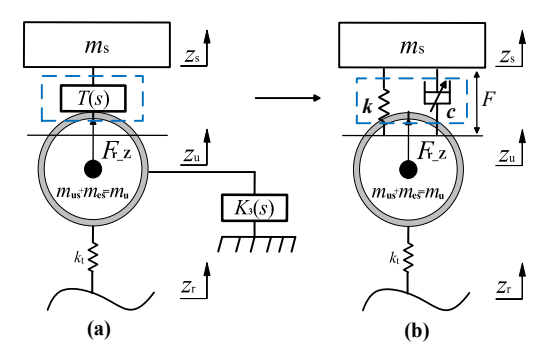


Figure 10. (a) Ideal quarter-vehicle suspension model based on the impedance transfer function for the third-order generalized ground-hook; (b) practical quarter-vehicle suspension model for the generalized ground-hook.

Based on the model shown in Figure 10b, the variation in the ideal generalized ground-hook's output force amplitude–frequency characteristics acting on the wheel is shown in Figure 11.

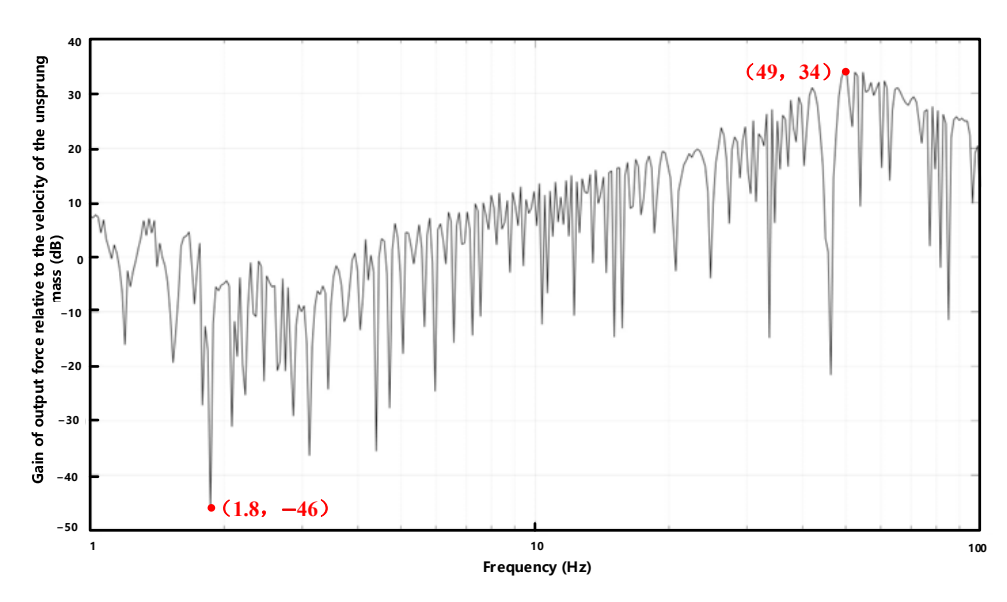


Figure 11. Variation in the suspension's output force amplitude–frequency characteristics under sinusoidal excitation, controlled by the third-order generalized ground-hook impedance transfer function.

As shown in Figure 11, the amplitude of the output force remained low in the low-frequency range (1–10 Hz), with a minimum peak of –46 dB at around 1.8 Hz. This indicates that the system had a weak amplification effect on the input excitation (the velocity of the unsprung mass) within this frequency band, demonstrating the system's strong suppression of low-frequency vibrations. Above 100 Hz, the amplitude increased sharply, peaking at +34 dB at around 49 Hz. This rapid increase in the amplitude indicates significant changes in the system's dynamic characteristics, especially in its damping and inertia, leading to a more pronounced amplification of the high-frequency components, thereby enhancing the system's response to high-frequency signals.

Under a sinusoidal road surface with an amplitude of 10 mm and a frequency range of [0.01–15] Hz, the ideal generalized ground-hook damping force is

$$F_{Ks} = K_3(s)\dot{z}_{u},\tag{15}$$

Machines 2025, 13, 556 18 of 28

Using the semi-active quarter-vehicle model shown in Figure 10b, the controllable damping force generated at both terminals of the semi-active damper can be expressed as

$$F_{\text{ctrl}} = c_{\text{ctrl}}(\dot{z}_{\text{s}} - \dot{z}_{\text{u}}), \tag{16}$$

where c_{ctrl} is the controllable damping coefficient. Suppose that we want the semi-active force to be equal to the ideal generalized ground-hook damping force:

$$F_{\text{ctrl}} = -F_{\text{Ks}}$$

$$c_{\text{ctrl}}(\dot{z}_{\text{s}} - \dot{z}_{\text{u}}) = -K_{3}(s)\dot{z}_{\text{u}},$$

$$c_{\text{ctrl}} = -\frac{K_{3}(s)\dot{z}_{\text{u}}}{(\dot{z}_{\text{s}} - \dot{z}_{\text{u}})}$$
(17)

Considering the constraint conditions of the adjustable damping coefficient of the semi-active damper, it also needs to satisfy

$$c_{\min} \le c_{\text{ctrl}} \le c_{\max},$$
 (18)

where c_{\min} is the minimum damping coefficient that the semi-active damper can provide, and c_{\max} is the maximum damping coefficient that the semi-active damper can provide.

To reduce the manufacturing costs of the damper and controller, a switch-type generalized ground-hook control using Equation (24) can be adopted to simplify the control rules. Among them, for $K_3(s)$, substituting the optimized parameters from Table 2, we obtain

$$K_3(s) = 20.3 \frac{s^3 + 365.6s^2 + 5s + 2400}{s^3 + 16598s^2 + 9216s + 3698.1}$$
(19)

Substituting $s = j\omega$ (where j is an imaginary unit and ω is the system's excitation angular frequency) and simplifying the result, we get

$$K_3(s) = 20.3 \frac{j\omega^3 + 365.6\omega^2 - 5j\omega - 2400}{j\omega^3 + 16598\omega^2 - 9216j\omega - 3698.1}$$
(20)

Eliminating the imaginary part, we get

$$K_3(s) = \frac{7421.68\omega^2 - 48720}{16598\omega^2 - 3698.1},\tag{21}$$

At this point, the controllable damping coefficient c_{ctrl} is

$$c_{\text{ctrl}} = -\frac{\dot{z}_{\text{u}}}{(\dot{z}_{\text{s}} - \dot{z}_{\text{u}})} \cdot \frac{7421.68\omega^2 - 48720}{16598\omega^2 - 3698.1},\tag{22}$$

For Equation (22), to obtain c_{max} , one must simultaneously satisfy the conditions $-\dot{z}_u(\dot{z}_s-\dot{z}_u)\geq 0$ and $(7421.68\omega^2-48720)\cdot(16598\omega^2-3698.1)\geq 0$, from which the range of ω can be derived as $\omega\geq 2.56$ or $0\leq \omega\leq 0.47$. Alternatively, one must simultaneously satisfy the conditions $-\dot{z}_u(\dot{z}_s-\dot{z}_u)\leq 0$ and $(7421.68\omega^2-48720)\cdot(16598\omega^2-3698.1)\leq 0$, yielding the range $0.47\leq \omega\leq 2.56$. Similarly, to obtain c_{min} , one must simultaneously satisfy the conditions $-\dot{z}_u(\dot{z}_s-\dot{z}_u)\geq 0$ and $(7421.68\omega^2-48720)\cdot(16598\omega^2-3698.1)\leq 0$, resulting in the range $0.47\leq \omega\leq 2.56$, or simultaneously satisfy the conditions $-\dot{z}_u(\dot{z}_s-\dot{z}_u)\leq 0$ and $(7421.68\omega^2-48720)\cdot(16598\omega^2-3698.1)\geq 0$, resulting in a range of $\omega\geq 2.56$ or $0\leq \omega\leq 0.47$.

Machines 2025, 13, 556 19 of 28

We obtain the criterion for judging the control rule:

$$c_{\text{ctrl}} = \begin{cases} c_{\text{max}}, -\dot{z}_{\text{u}}(\dot{z}_{\text{s}} - \dot{z}_{\text{u}}) \ge 0 \& \omega \ge 2.56 \\ c_{\text{max}}, -\dot{z}_{\text{u}}(\dot{z}_{\text{s}} - \dot{z}_{\text{u}}) \ge 0 \& 0 \le \omega \le 0.47 \\ c_{\text{max}}, -\dot{z}_{\text{u}}(\dot{z}_{\text{s}} - \dot{z}_{\text{u}}) \le 0 \& 0.47 \le \omega \le 2.56 \\ c_{\text{min}}, -\dot{z}_{\text{u}}(\dot{z}_{\text{s}} - \dot{z}_{\text{u}}) \ge 0 \& 0.47 \le \omega \le 2.56 \\ c_{\text{min}}, -\dot{z}_{\text{u}}(\dot{z}_{\text{s}} - \dot{z}_{\text{u}}) \le 0 \& \omega \ge 2.56 \\ c_{\text{min}}, -\dot{z}_{\text{u}}(\dot{z}_{\text{s}} - \dot{z}_{\text{u}}) \le 0 \& 0 \le \omega \le 0.47 \end{cases}$$

$$(23)$$

Based on the analysis of the relationship between the Laplace transform and Fourier transform, it can be derived that $\omega=2\pi f=2\pi vn$ (where n represents the pavement spatial frequency of 0.1 cycles/m and the vehicle speed v is 20 m/s), and after substituting these parameters, we obtain $\omega=12.57$ rad/s. From this, it can be observed that the road surface spatial frequency n and vehicle speed v directly influence the magnitude of the angular frequency v. From Equation (23), it is also evident that the magnitude of the angular frequency v0 directly determines the selection of the final control rule. After rearrangement, the final criterion for determining the control rule is

$$c_{\text{ctrl}} = \begin{cases} c_{\text{max}}, -\dot{z}_{\mathbf{u}}(\dot{z}_{\mathbf{s}} - \dot{z}_{\mathbf{u}}) \ge 0 \\ c_{\text{min}}, -\dot{z}_{\mathbf{u}}(\dot{z}_{\mathbf{s}} - \dot{z}_{\mathbf{u}}) \le 0 \end{cases}$$
(24)

A semi-active control model was established based on its dynamic equations, from which we obtained $c_{\rm max}=4495.63~{\rm N\cdot s/m}$ and $c_{\rm min}=3.78~{\rm N\cdot s/m}$ through optimization and which ultimately yielded time-domain comparison diagrams of the suspension performance indicators.

As shown in Figure 12, after adopting a semi-active control strategy, the system's various dynamic response indicators exhibited differential characteristics: the deviation between the dynamic tire load spectrum and the theoretically predicted value was relatively significant, and notable deviations also existed in the body acceleration and suspension working space. To investigate the mechanism behind these deviations and enhance the control precision, our subsequent research will delve into an in-depth analysis based on the frequency-domain response characteristics, examining the influence mechanism of the phase lag effects on the system's dynamic properties and subsequently establishing a phase compensation control framework.

5.2. The Analysis of the Phase–Frequency Characteristics of the HMDV Generalized Ground-Hook Dynamic Inertial Suspension

The aforementioned research results show significant systematic deviations in both the body acceleration and dynamic tire load parameters after implementing the semi-active control strategy. Because of this, this study proposed to expand the traditional spring—damper parallel suspension structure into eight paradigmatic topological structures (as shown in Figure 13). By establishing the transfer functions between the wheel velocity and the relative velocity of the suspension motion for each structure, we systematically analyzed their phase—frequency response characteristics, aiming to reconstruct the parameter tuning space of the semi-active control algorithm and ultimately achieve the collaborative optimization of the dynamic characteristics of the control strategy and the frequency-domain response characteristics of the suspension system.

Machines 2025, 13, 556 20 of 28

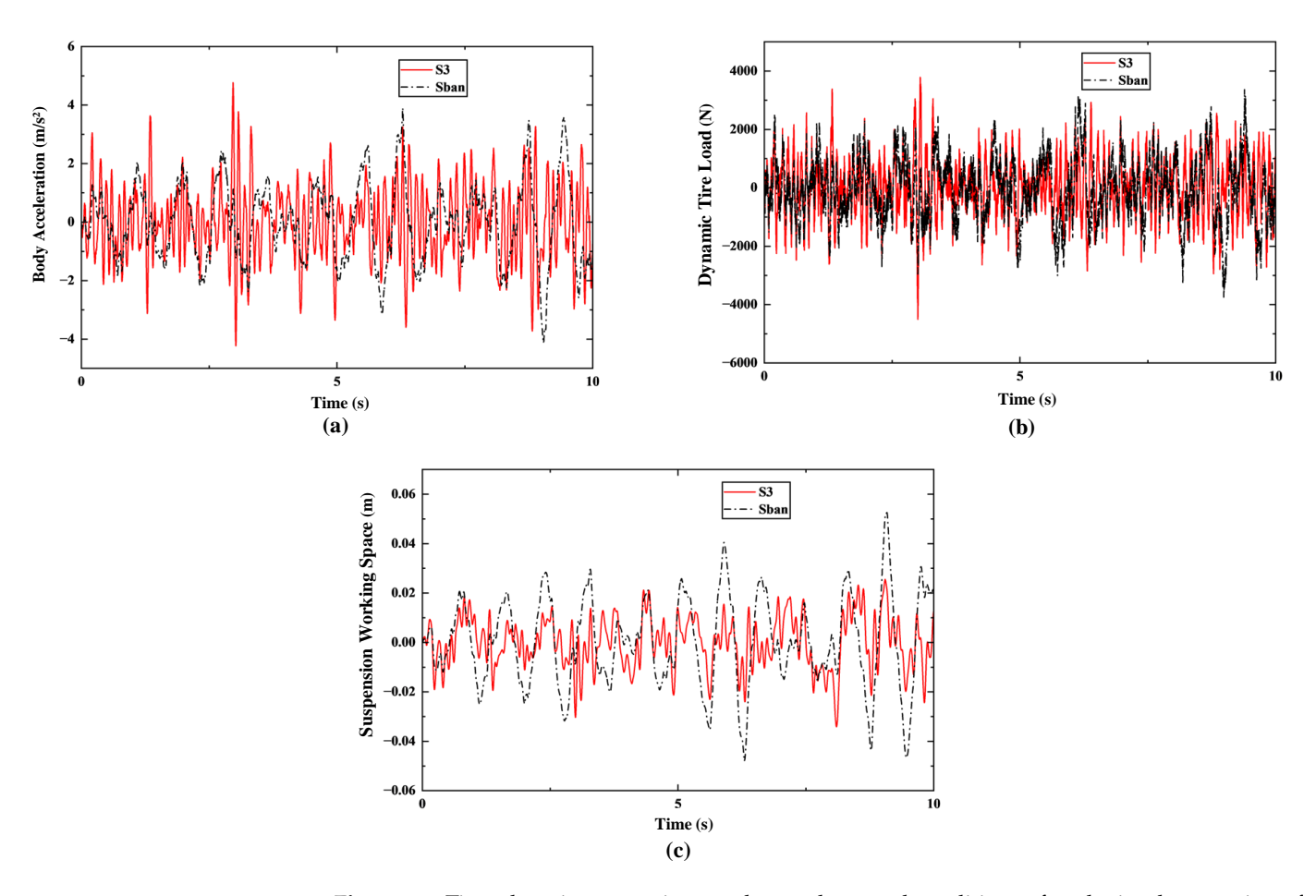


Figure 12. Time-domain comparison under random road conditions after the implementation of semi-active control: (a) body acceleration, (b) dynamic tire load, (c) suspension working space.

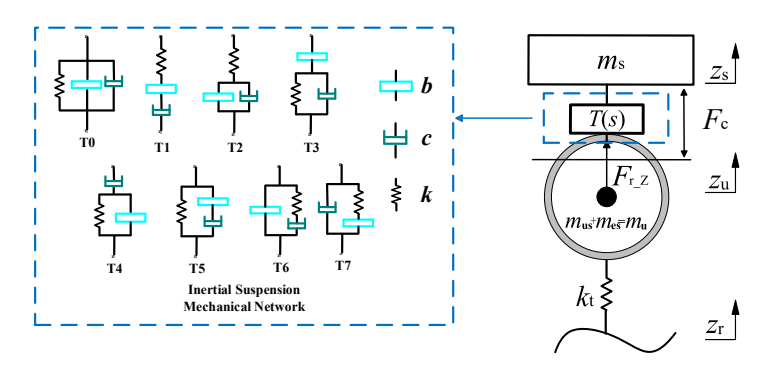


Figure 13. Specific implementation of a suspension system, T(s), controlled by the generalized ground-hook impedance transfer function.

The Laplace equation for the suspension dynamics in Figure 13 is shown in Equation (25):

$$\begin{cases}
 m_2 s^2 X_2 + sT(s)(X_2 - X_1) = 0 \\
 m_1 s^2 X_1 - sT(s)(X_2 - X_1) + sK(s)X_1 + k_t(X_1 - X_r) = 0'
\end{cases}$$
(25)

where X_2 , X_1 , and X_r are the Laplace transforms of z_s , z_u , and z_r , respectively. According to Equation (25), the transfer function of the body acceleration z_s to the road vertical input displacement z_r is

$$H_{\tilde{z}_{s} \sim z_{r}}(s) = \frac{X_{2}}{X_{r}} s^{2}$$

$$= \frac{k_{t} T(s) s^{2}}{m_{u} m_{s} s^{3} + (m_{u} + m_{s}) T(s) s^{2} + m_{s} K(s) s^{2} + T(s) K(s) s + k_{t} (m_{s} s + T(s))}$$
(26)

Machines 2025, 13, 556 21 of 28

The transfer function of the suspension working space $(z_s - z_u)$ to the road vertical input displacement x_r is

$$H_{(z_{s}-z_{u})\sim z_{r}}(s) = \frac{X_{2}-X_{1}}{X_{r}}s^{2}$$

$$= \frac{-k_{t}m_{s}s^{2}}{m_{u}m_{s}s^{3}+(m_{u}+m_{s})T(s)s^{2}+m_{s}K(s)s^{2}+T(s)K(s)s+k_{t}(m_{s}s+T(s))}$$
(27)

The transfer function of the dynamic tire load $(z_u - z_r)k_t$ to the road vertical input displacement z_r is

$$H_{(z_{u}-z_{r})k_{t}\sim z_{r}}(s) = \frac{X_{1}-X_{r}}{X_{r}}k_{t}$$

$$= \frac{-k_{t}(m_{u}m_{s}s^{3}+(m_{u}+m_{s})T(s)s^{2}+m_{s}K(s)s^{2}+T(s)K(s)s)}{m_{u}m_{s}s^{3}+(m_{u}+m_{s})T(s)s^{2}+m_{s}K(s)s^{2}+T(s)K(s)s+k_{t}(m_{s}s+T(s))}$$
(28)

The transfer function of the wheel speed relative to the suspension movement can be further obtained as

$$H_{\dot{z}_{\mathbf{u}} \sim (\dot{z}_{\mathbf{s}} - \dot{z}_{\mathbf{u}})}(s) = -\frac{m_{\mathbf{s}}s + T(s)}{m_{\mathbf{s}}s},$$
 (29)

Based on the eight structures of T(s) shown in Figure 13, write the impedance expressions for the topological structures of the inertial suspension:

$$T_0(s) = bs + c + \frac{k}{s},$$
 (30)

$$T_1(s) = \frac{1}{\frac{s}{k} + \frac{1}{c} + \frac{1}{bs}} = \frac{kbcs}{bcs^2 + bks + ck'}$$
(31)

$$T_2(s) = \frac{1}{\frac{s}{k} + \frac{1}{bs + c}} = \frac{bks + ck}{bs^2 + cs + k'}$$
(32)

$$T_3(s) = \frac{1}{\frac{1}{bs} + \frac{1}{\frac{k}{s} + c}} = \frac{bcs^2 + bks}{bs^2 + cs + k'}$$
(33)

$$T_4(s) = \frac{1}{\frac{1}{c} + \frac{1}{\frac{k}{2} + bs}} = \frac{bcs^2 + ck}{bs^2 + cs + k'}$$
(34)

$$T_5(s) = \frac{k}{s} + \frac{1}{\frac{1}{1c} + \frac{1}{c}} = \frac{bcs^2 + bks + ck}{bs^2 + cs},$$
(35)

$$T_6(s) = bs + \frac{1}{\frac{s}{k} + \frac{1}{c}} = \frac{bcs^2 + bks + ck}{cs + k},$$
 (36)

$$T_7(s) = c + \frac{1}{\frac{s}{k} + \frac{1}{hs}} = \frac{bcs^2 + bks + kc}{bs^2 + k},$$
 (37)

where $T_0(s)$, $T_1(s)$, $T_2(s)$, $T_3(s)$, $T_4(s)$, $T_5(s)$, $T_6(s)$, and $T_7(s)$ are the impedance expressions for the structures T0, T1, T2, T3, T4, T5, T6, and T7, respectively. Subsequently, by substituting these eight impedance expressions into Equation (29), the transfer functions of the wheel speed relative to the suspension motion for these structures can be obtained individually. The phase–frequency characteristics can be studied using these transfer functions, as illustrated in Figures 14 and 15.

Machines 2025, 13, 556 22 of 28

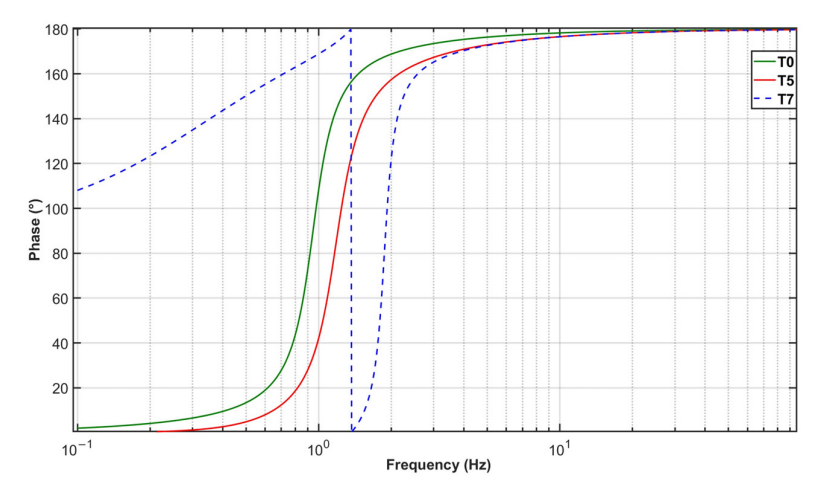


Figure 14. Phase–frequency characteristics of the generalized ground-hook control logic for the structures T0, T5, and T7.

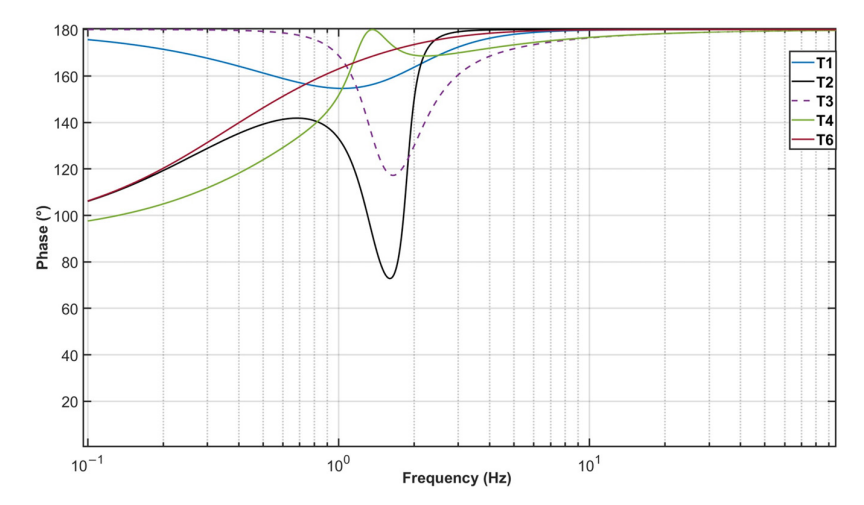


Figure 15. Phase–frequency characteristics of the generalized ground-hook control logic for the structures T1, T2, T3, T4, and T6.

According to the existing research results [54], to improve a vehicle's ride comfort and road-friendliness, the logic of the generalized ground-hook control strategy should conform to the following: in the low-frequency range, the ground-hook damping and ground-hook inertance should operate at low parameter values, and at this time, there should be no phase difference between the wheel velocity and the relative velocity of the suspension motion; in the high-frequency range, the opposite should apply. As can be seen from Figures 14 and 15, only the T0 and T5 structures conformed to the control logic.

5.3. Deviation Correction After Semi-Active Control of HMDV Generalized Ground-Hook Dynamic Inertial Suspension

First, the deviation range of various indicators after applying semi-active control using the T0 structure was researched, and the system dynamic equation for the T0 structure was established. The T0 structural model is illustrated in Figure 16.

$$\begin{cases}
 m_{s}\ddot{z}_{s} + k(z_{s} - z_{u}) + c(\dot{z}_{s} - \dot{z}_{u}) + b(\ddot{z}_{s} - \ddot{z}_{u}) = 0 \\
 (m_{us} + m_{es})\ddot{z}_{u} + k_{t}(z_{u} - z_{r}) - k(z_{s} - z_{u}) - c(\dot{z}_{s} - \dot{z}_{u}) - b(\ddot{z}_{s} - \ddot{z}_{u}) + F_{ctrl} + F_{r_{z}} = 0'
\end{cases}$$
(38)

Machines 2025, 13, 556 23 of 28

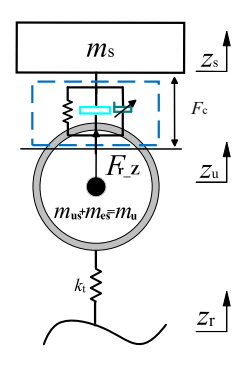


Figure 16. Generalized ground-hook suspension system with semi-active control utilizing T0 structure.

Based on its dynamic equation, we established a semi-active control model, obtained $c_{\text{max}} = 98.7 \, \text{N·s/m}$, $c_{\text{min}} = 47.36 \, \text{N·s/m}$, and $b = 30 \, \text{kg}$ through optimization, and obtained a time-domain comparison diagram of the suspension performance indicators, as shown in Figure 17.

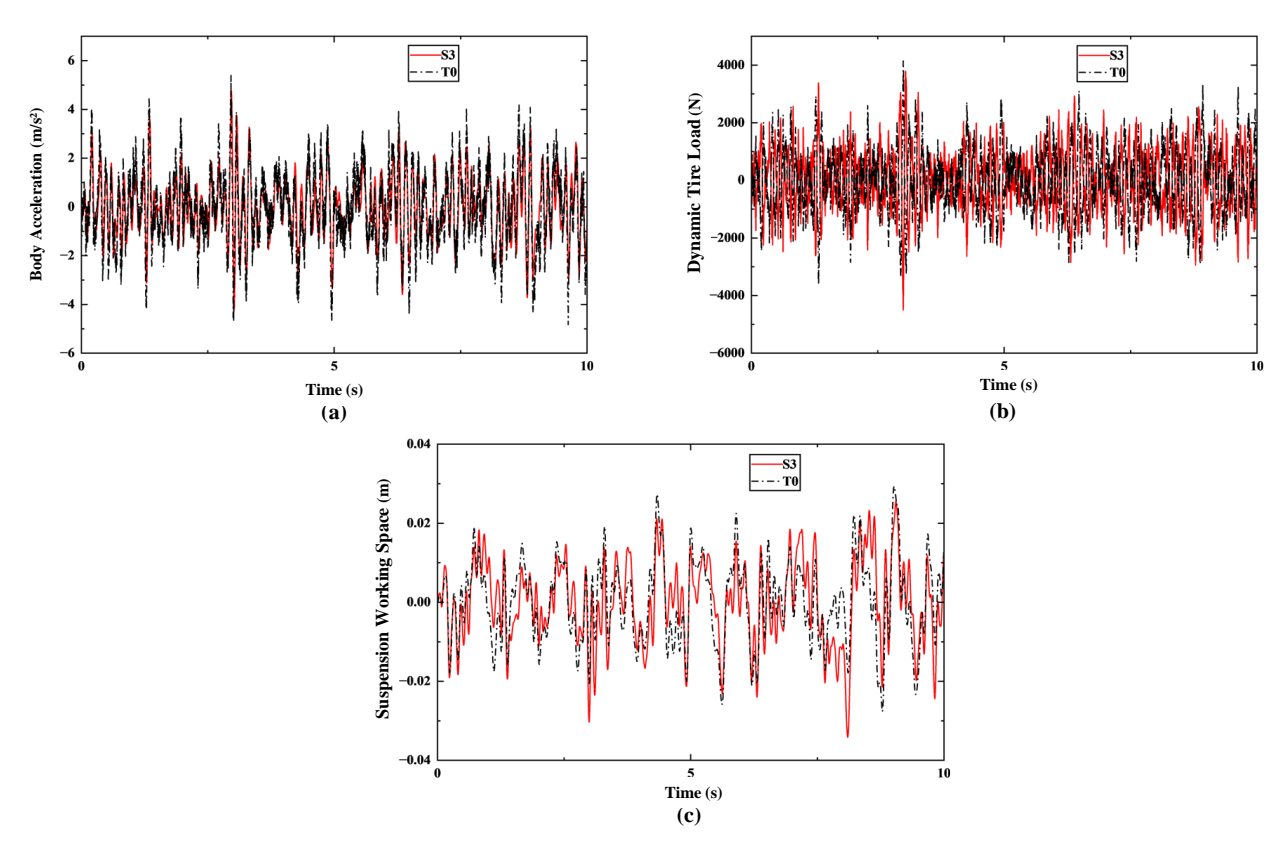


Figure 17. Time-domain comparison of suspension performance indicators after adopting T0 semi-active control structure: (a) body acceleration, (b) dynamic tire load, (c) suspension working space.

Next, we constructed the dynamic equation of the T5 structure. The inerter was connected to the vehicle body, where it interacted with the sprung mass velocity. At the opposite end, the damper was subjected to the unsprung mass velocity. This configuration led to the development of a velocity at the intermediate point between the inerter and the damper (where z_3 represents the middle displacement of the two elements). The T5 structural model is illustrated in Figure 18.

$$\begin{cases}
 m_{s}\ddot{z}_{s} + k(z_{s} - z_{u}) + b(\ddot{z}_{s} - \ddot{z}_{3}) = 0 \\
 b(\ddot{z}_{s} - \ddot{z}_{3}) + c(\dot{z}_{u} - \dot{z}_{3}) = 0 \\
 (m_{us} + m_{es})\ddot{z}_{u} + k_{t}(z_{u} - z_{r}) + k(z_{u} - z_{s}) + c(\dot{z}_{u} - \dot{z}_{3}) + F_{ctrl} + F_{r_{z}} = 0
\end{cases} , (39)$$

Machines 2025, 13, 556 24 of 28

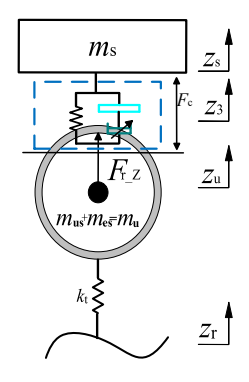


Figure 18. Generalized ground-hook suspension system with semi-active control utilizing T5 structure.

For T5-structured semi-active control systems with intermediate displacement states, the governing control rule is defined as

$$c_{\text{ctrl}} = \begin{cases} c_{\text{max}}, -\dot{z}_u(\dot{z}_3 - \dot{z}_u) \ge 0 \\ c_{\text{min}}, -\dot{z}_u(\dot{z}_3 - \dot{z}_u) \le 0 \end{cases}$$
(40)

Based on its dynamic equations, a semi-active control model was established. We obtained $c_{\rm max}=200~{\rm N\cdot s/m}$, $c_{\rm min}=111~{\rm N\cdot s/m}$, and $b=40~{\rm kg}$ through optimization. Ultimately, a time-domain comparison chart of the suspension performance indicators was generated, as shown in Figure 19.

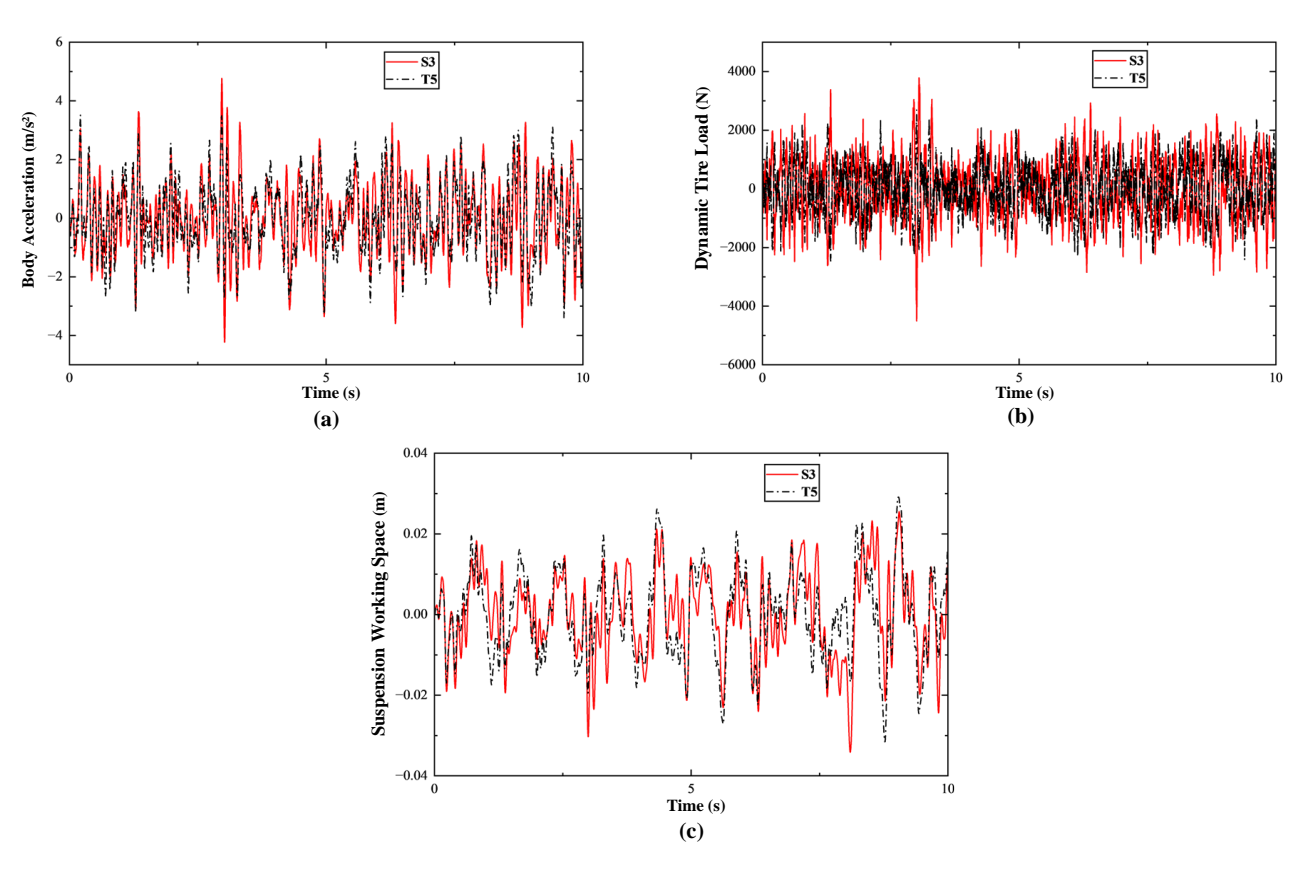


Figure 19. Time-domain comparison of suspension performance indicators after adopting T5 semi-active control structure: (a) body acceleration, (b) dynamic tire load, (c) suspension working space.

Based on the comparative deviation analysis of the multi-dimensional performance indicators for the suspension system, as shown in Figure 20, it can be observed that when employing the semi-active control strategy with the T5 structure, the deviation

Machines **2025**, 13, 556 25 of 28

amplitudes were notably lower than those of the other two semi-active control schemes for key parameters such as the body acceleration, dynamic tire load, and suspension working space. Quantitative analysis indicated that this control strategy exhibited a high degree of time-domain consistency with the theoretical response of the ideal third-order generalized ground-hook impedance transfer function control, verifying that the T5 structure could achieve the progressive approximation of higher-order impedance characteristics while ensuring the effective operation of the damper. This provides a more practically realizable solution for optimizing the comprehensive performance of suspension systems under complex operating conditions.

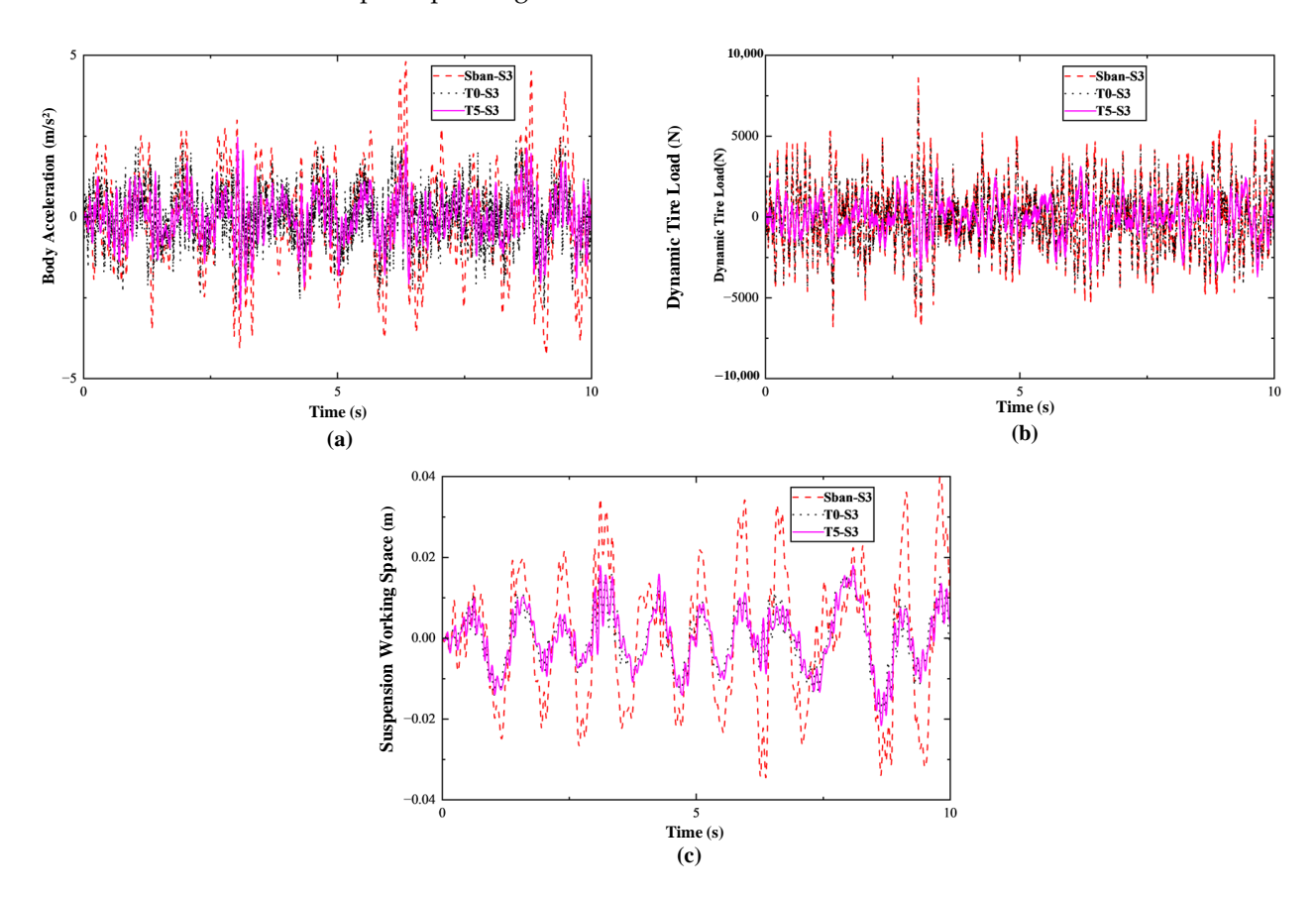


Figure 20. Time-domain comparative analysis of suspension performance indicators' deviations under three semi-active control strategies: (a) body acceleration, (b) dynamic tire load, (c) suspension working space.

6. Results

The deterioration in the vehicle dynamics caused by an increased unsprung mass and the disturbance of unbalanced radial electromagnetic forces in HMDVs has become a critical bottleneck restricting their large-scale application. This paper proposes a generalized ground-hook control strategy based on the reconstruction of an impedance transfer function, addressing the contradictory defects of traditional ground-hook control in optimizing the dynamic tire load and decreasing the body acceleration. The study systematically revealed the regulation laws of first-order to fifth-order generalized ground-hook impedance transfer functions on multi-dimensional suspension performance indicators by establishing a quarter-vehicle suspension coupled dynamic model that incorporated the electromagnetic characteristics of a switched reluctance motor. The research found that the third-order transfer function control could reduce the dynamic tire load by 8% and the suspension working space by 22% while maintaining a slight optimization of the body acceleration. Additionally, the strategy retained an optimized computational balance, showing marginally

Machines **2025**, 13, 556 26 of 28

higher complexity than lower-order approaches yet substantially lower complexity than higher-order structures, fully satisfying the real-time operational constraints and achieving Pareto optimality between the control accuracy and real-time performance.

Since the ideal generalized ground-hook dynamic inertial suspension system cannot be directly applied to vehicles, this study pioneered an innovative implementation framework for generalized ground-hook control using semi-active control strategies. However, it was found that after implementing the semi-active control strategy, significant systematic deviations appeared in the parameters of the body acceleration, dynamic tire load, and suspension working space. Because of this, this study proposed expanding the traditional spring-damper parallel suspension structure into eight paradigmatic topological structures. By establishing transfer functions for the relative velocities of the wheel speed and suspension motion for each structure, their phase-frequency response characteristics were systematically analyzed to reconstruct the parameter tuning space for the semi-active control algorithm, ultimately achieving coordinated optimization between the dynamic characteristics of the control strategy and the frequency-domain response characteristics of the suspension system. Based on the logic of the generalized ground-hook control strategy, the T0 and T5 structures were found to conform to the control logic and screened out. Finally, through a time-domain comparison of the suspension performance indicators, it was concluded that semi-active control using the T5 structure was closer to the ideal third-order generalized ground-hook impedance transfer function control.

In future research, we plan to employ magnetorheological (MR) dampers [55,56] to implement semi-active control strategies, with a particular focus on investigating the impact of magnetic field variation rates on the system performance and the real-time responsiveness of the control system.

Author Contributions: Conceptualization, Y.P. and S.Z.; methodology, Y.Y.; software, Y.P.; validation, Y.P., S.D. and J.H.; formal analysis, S.Z.; investigation, S.D.; resources, X.Y.; data curation, Y.P.; writing—original draft preparation, Y.P.; writing—review and editing, Y.S. and Y.Y.; visualization, Y.P.; supervision, X.Y.; project administration, X.Y.; funding acquisition, X.Y. All authors have read and agreed to the published version of the manuscript.

Funding: This research was supported by the National Natural Science Foundation of China (Grant No. 52202471), the Young Elite Scientists Sponsorship Program run by CAST (Grant No. 2022QNRC001), and the Qing Lan Project of Jiangsu Province.

Data Availability Statement: The original contributions presented in this study are included in the article.

Conflicts of Interest: The authors declare no conflict of interest.

Abbreviations

The following abbreviations are used in this manuscript:

HMDV hub motor-driven vehicle PSD power spectral density SRM switched reluctance motor

RMS root mean square MR magnetorheological

References

- 1. Mok, Y.M.; Zhai, L.; Wang, C.; Zhang, X.; Hou, Y. A post impact stability control for four hub-motor independent-drive electric vehicles. *IEEE Trans. Veh. Technol.* **2021**, *71*, 1384–1396. [CrossRef]
- 2. Wu, H.; Zheng, L.; Li, Y. Coupling effects in hub motor and optimization for active suspension system to improve the vehicle and the motor performance. *J. Sound Vib.* **2020**, 482, 115426. [CrossRef]

Machines **2025**, 13, 556 27 of 28

3. Wang, J.; Gao, S.; Qiang, Y.; Xu, M.; Guan, C.; Zhou, Z. Structural topology and dynamic response analysis of an electric torque vectoring drive-axle for electric vehicles. *Automot. Innov.* **2022**, *5*, 164–179. [CrossRef]

- 4. Hengst, J.; Werra, M.; Küçükay, F. Evaluation of transmission losses of various battery electric vehicles. *Automot. Innov.* **2022**, *5*, 388–399. [CrossRef]
- 5. Liu, Y.; Chen, L.; Cai, T.; Sun, W.; Xu, X.; Wang, S. Dual-pump Control Algorithm of Two-speed Powershift Transmissions in Electric Vehicles. *Automot. Innov.* **2022**, *5*, 57–69. [CrossRef]
- 6. Huang, T.; Wang, J.; Pan, H.; Sun, W. Finite-time fault-tolerant integrated motion control for autonomous vehicles with prescribed performance. *IEEE Trans. Transp. Electrif.* **2022**, *9*, 4255–4265. [CrossRef]
- 7. Miranda, M.H.; Silva, F.L.; Lourenço, M.A.; Eckert, J.J.; Silva, L.C. Electric vehicle powertrain and fuzzy controller optimization using a planar dynamics simulation based on a real-world driving cycle. *Energy* **2022**, 238, 121979. [CrossRef]
- 8. Saravanakumar, D.; Sakthivel, G.; Jegadeeshwaran, R.; Pathi, J.L.; Kumar, M.M.; Muthuramalingam, T. Assessment of vehicle handling performance of drivers using machine learning algorithms. *IEEE Access* **2022**, *10*, 132288–132297. [CrossRef]
- 9. Feng, H.; Tao, Y.; Feng, J.; Zhang, Y.; Xue, H.; Wang, T.; Xu, X.; Chen, P. Fault-Tolerant Collaborative Control of Four-Wheel-Drive Electric Vehicle for One or More In-Wheel Motors' Faults. *Sensors* **2025**, *25*, 1540. [CrossRef]
- 10. Tao, Y.; Ge, C.; Feng, H.; Xue, H.; Yao, M.; Tang, H.; Liao, Z.; Chen, P. A Novel Approach for Adaptively Separating and Extracting Compound Fault Features of the In-wheel Motor Bearing. *ISA Trans.* **2025**, *159*, 337–351. [CrossRef]
- 11. Li, Y.; Yang, X.; Shen, Y.; Liu, Y.; Wang, W. Optimal design and dynamic control of the HMDV inertial suspension based on the ground-hook positive real network. *Adv. Eng. Softw.* **2022**, *171*, 103171. [CrossRef]
- 12. Yang, X.; Song, H.; Shen, Y.; Liu, Y. Study on adverse effect suppression of hub motor driven vehicles with inertial suspensions. *Proc. Inst. Mech. Eng. Part D-J. Automob. Eng.* **2022**, 236, 767–779. [CrossRef]
- 13. Wang, S.; Xu, X.; Chen, X.; Li, R. Lightweight design of the planetary gear reducer of reduction drive hub motors. *J. Phys. Conf. Ser.* **2022**, 2338, 012059. [CrossRef]
- 14. Deng, Z.; Luo, X.; Liao, X.; Li, X.; Du, Z.; Hou, M.; Wei, H. Analysis and suppression of the negative effect of electromagnetic characteristics of wheel hub motor drive system on vehicle dynamics performance. *Nonlinear Dyn.* 2025, 113, 4425–4445. [CrossRef]
- 15. Cui, L.; Mao, H.; Xue, X.; Ding, S.; Qiao, B. Optimized design and test for a pendulum suspension of the crop spray boom in dynamic conditions based on a six DOF motion simulator. *Int. J. Agric. Biol. Eng.* **2018**, *11*, 76–85.
- 16. Cui, L.; Xue, X.; Le, F.; Mao, H.; Ding, S. Design and experiment of electro hydraulic active suspension for controlling the rolling motion of spray boom. *Int. J. Agric. Biol. Eng.* **2019**, *12*, 72–81. [CrossRef]
- 17. Shen, Y.; Li, J.; Huang, R.; Yang, X.; Chen, J.; Chen, L.; Li, M. Vibration control of vehicle ISD suspension based on the fractional-order SH-GH stragety. *Mech. Syst. Signal Process.* **2025**, 234, 112880. [CrossRef]
- 18. Shen, Y.; Li, Z.; Tian, X.; Ji, K.; Yang, X. Vibration Suppression of the Vehicle Mechatronic ISD Suspension Using the Fractional-Order Biquadratic Electrical Network. *Fractal Fract.* **2025**, *9*, 106. [CrossRef]
- 19. Yang, X.; Zhang, T.; Shen, Y.; Liu, Y.; Bui, V.; Qiu, D. Tradeoff analysis of the energy-harvesting vehicle suspension system employing inerter element. *Energy* **2024**, *308*, 132841. [CrossRef]
- 20. Yuexia, C.; Long, C.; Wang, R.; Xing, X.; Yujie, S.; Yanling, L. Modeling and test on height adjustment system of electrically-controlled air suspension for agricultural vehicles. *Int. J. Agric. Biol. Eng.* **2016**, *9*, 40–47.
- 21. Smith, M.C. Synthesis of mechanical networks: The inerter. IEEE Trans. Autom. Control 2002, 47, 1648–1662. [CrossRef]
- 22. Chen, Z.; Lai, S.-K.; Yang, Z.; Ni, Y.-Q.; Yang, Z.; Cheung, K.C. AT-PINN-HC: A refined time-sequential method incorporating hard-constraint strategies for predicting structural behavior under dynamic loads. *Comput. Methods Appl. Mech. Eng.* 2025, 436, 117691. [CrossRef]
- 23. Valá ek, M.; Stejskal, V.; ika, Z.; Vaculin, O. Control concepts of semi-active damping of truck suspension for road friendliness. *Veh. Syst. Dyn.* **1998**, 29, 766–771.
- 24. Feng, Y.; Zhu, J.; Chai, H.; He, W.; Huang, L.; Wang, W. Impedance-Based Multimodal Electrical-Mechanical Intrinsic Flow Cytometry. *Small* **2023**, *19*, e2303416. [CrossRef]
- 25. Parida, L.; Moharana, S.; Ferreira, V.M.; Giri, S.K.; Ascensão, G. A novel CNN-LSTM hybrid model for prediction of electromechanical impedance signal based bond strength monitoring. *Sensors* **2022**, 22, 9920. [CrossRef]
- 26. Tenreiro, A.F.G.; Lopes, A.M.; da Silva, L.F. A review of structural health monitoring of bonded structures using electromechanical impedance spectroscopy. *Struct. Health Monit.* **2022**, 21, 228–249. [CrossRef]
- 27. Bai, M.; Wang, J.; Sun, W. Coupled Control of Preview Active Suspension and Longitudinal Dynamics for Autonomous Vehicle. *IEEE Trans. Syst. Man Cybern. Syst.* 2025, 55, 4656–4669. [CrossRef]
- 28. Chen, G.; Du, G.; Xia, J.; Xie, X.; Wang, Z. Aperiodic Sampled-Data Control of Vehicle Active Suspension System: An Uncertain Discrete-Time Model Approach. *IEEE Trans. Ind. Inform.* **2024**, 20, 6739–6750. [CrossRef]
- 29. Yu, M.; Evangelou, S.A.; Dini, D. Advances in active suspension systems for road vehicles. *Engineering* **2024**, *33*, 160–177. [CrossRef]
- 30. Fu, B.; Liu, B.; Di Gialleonardo, E.; Bruni, S. Semi-active control of primary suspensions to improve ride quality in a high-speed railway vehicle. *Veh. Syst. Dyn.* **2023**, *61*, 2664–2688. [CrossRef]

Machines 2025, 13, 556 28 of 28

31. Ricco, M.; Alshawi, A.; Gruber, P.; Dhaens, M.; Sorniotti, A. Nonlinear model predictive control for yaw rate and body motion control through semi-active and active suspensions. *Veh. Syst. Dyn.* **2024**, *62*, 1587–1620. [CrossRef]

- 32. Li, T.; Liao, Z.; Cai, Y. Physical modeling for digital twin of Continuous Damping Control damper. *J. Manuf. Process.* **2023**, *99*, 96–104. [CrossRef]
- 33. Peng, T.; Chen, J.; Wang, S. Analysis and design of adjustable-gap double-side axial flux permanent magnet hysteresis damper. *IEEE Trans. Ind. Electron.* **2023**, *71*, 3514–3524. [CrossRef]
- 34. Shmerling, A.; Gerdts, M. Short-horizon acceleration-predictive control for reducing lateral seismic inertia forces of inelastic frame structures using semi-active fluid viscous dampers. *Comput. Struct.* **2023**, *281*, 107032. [CrossRef]
- 35. Liu, C.; Lai, S.-K.; Ni, Y.-Q.; Chen, L. Dynamic modelling and analysis of a physics-driven strategy for vibration control of railway vehicles. *Veh. Syst. Dyn.* **2025**, *63*, 1080–1110. [CrossRef]
- 36. Saitoh, S. Hilbert spaces induced by Hilbert space valued functions. Proc. Am. Math. Soc. 1983, 89, 74–78. [CrossRef]
- 37. O'Connell, T.C.; Wells, J.R.; Watts, O. A lumped-parameter off-axis-capable dynamic switched reluctance machine model including unbalanced radial forces. *IEEE Trans. Energy Convers.* **2014**, *30*, 161–174. [CrossRef]
- 38. Deng, Z.; Li, X.; Liu, T.; Zhao, S. Modeling and suppression of unbalanced radial force for in-wheel motor driving system. *J. Vib. Control* **2022**, *28*, 3108–3119. [CrossRef]
- 39. Deng, Z.; Ma, T. Analytical Model for Evaluating Unbalanced Electromagnetic Forces in Switched Reluctance Hub Motors Under Air-Gap Eccentricity; SAE Technical Paper; SAE International: Warrendale, PA, USA, 2024; pp. 2320–2345.
- 40. Hu, S.; Zuo, S.; Liu, M.; Wu, H.; Liu, Z. Modeling and analysis of radial electromagnetic force and vibroacoustic behaviour in switched reluctance motors. *Mech. Syst. Signal Process.* **2020**, 142, 106778. [CrossRef]
- 41. Li, Z.; Liu, L.; Wang, P.; Liu, Y.; Wei, X.; Xu, Q.; Sun, H. Modeling and analysis of radial electromagnetic force and vibration characteristics based on deflection dual-stator switched reluctance generator. *Micromachines* **2022**, *13*, 1494. [CrossRef]
- 42. Liu, Z.; Wu, X.; Cai, J.; Yang, Y.; Liu, C. Decoupled Topologies and Radial Levitation Control of a Novel Permanent Magnet Biased Bearingless Switched Reluctance Motor. *IEEE Trans. Ind. Electron.* **2024**, 72, 3370–3380. [CrossRef]
- 43. Ma, T.; Deng, Z.; Liu, W.; Hou, M. A Numerical Method to Determine the Radial Electromagnetic Force of the Switched Reluctance Motor Under Air Gap Eccentricity. *Machines* **2024**, *12*, 823. [CrossRef]
- 44. Wang, Z.; Cao, X.; Deng, Z.; Li, K. Modeling and characteristic investigation of axial reluctance force for bearingless switched reluctance motor. *IEEE Trans. Ind. Appl.* **2021**, *57*, 5215–5226. [CrossRef]
- 45. He, Y.-L.; Li, Y.; Zhang, W.; Xu, M.-X.; Bai, Y.-F.; Wang, X.-L.; Shi, S.-Z.; Gerada, D. Analysis of stator vibration characteristics in synchronous generators considering inclined static air gap eccentricity. *IEEE Access* **2022**, *11*, 7794–7807. [CrossRef]
- 46. Zhang, H.; Liu, Y.; Teng, W.; Song, S.; Wang, Y. Dynamic characteristics analysis of energy storage flywheel motor rotor with air-gap eccentricity fault. *J. Energy Storage* **2024**, *89*, 111684. [CrossRef]
- 47. Zhu, R.; Tong, X.; Han, Q.; He, K.; Wang, X.; Wang, X. Calculation and analysis of unbalanced magnetic pull of rotor under motor air gap eccentricity fault. *Sustainability* **2023**, *15*, 8537. [CrossRef]
- 48. Yang, Y.; Liu, C.; Lai, S.-K.; Chen, Z.; Chen, L. Frequency-dependent equivalent impedance analysis for optimizing vehicle inertial suspensions. *Nonlinear Dyn.* **2025**, *113*, 9373–9398. [CrossRef]
- 49. Xu, S.; He, B. A compliance modeling method of flexible rotary joint for collaborative robot using passive network synthesis theory. *Proc. Inst. Mech. Eng. Part C J. Mech. Eng. Sci.* **2022**, 236, 4038–4048. [CrossRef]
- 50. Pourpanah, F.; Wang, R.; Lim, C.P.; Wang, X.-Z.; Yazdani, D. A review of artificial fish swarm algorithms: Recent advances and applications. *Artif. Intell. Rev.* **2023**, *56*, 1867–1903. [CrossRef]
- 51. Zhao, W.; Gu, L.; Dong, M. Application of artificial fish swarm algorithm in LQR control for active suspension. In Proceedings of the 2022 13th Asian Control Conference (ASCC), Jeju, Republic of Korea, 4–7 May 2022; pp. 2406–2409.
- 52. Mirza, A.F.; Mansoor, M.; Usman, M.; Ling, Q. Hybrid Inception-embedded deep neural network ResNet for short and medium-term PV-Wind forecasting. *Energy Convers. Manag.* **2023**, 294, 117574. [CrossRef]
- 53. *ISO 8608*; Mechanical Vibration—Road Surface Profiles—Reporting of Measured Data. International Standards Organisation: Geneve, Switzerland, 2016.
- 54. Yang, Y.; Liu, C.; Chen, L.; Zhang, X. Phase deviation of semi-active suspension control and its compensation with inertial suspension. *Acta Mech. Sin.* **2024**, *40*, 523367. [CrossRef]
- 55. Makowski, M.; Knap, L. Reduction of wheel force variations with magnetorheological devices. J. Vib. Control 2014, 20, 1552–1564. [CrossRef]
- 56. Strecker, Z.; Roupec, J.; Mazurek, I.; Machacek, O.; Kubik, M.; Klapka, M. Design of magnetorheological damper with short time response. *J. Intell. Mater. Syst. Struct.* **2015**, 26, 1951–1958. [CrossRef]

Disclaimer/Publisher's Note: The statements, opinions and data contained in all publications are solely those of the individual author(s) and contributor(s) and not of MDPI and/or the editor(s). MDPI and/or the editor(s) disclaim responsibility for any injury to people or property resulting from any ideas, methods, instructions or products referred to in the content.